










Rapid disc settling and the transition from bursty to steady star formation in Milky Way-mass galaxies

Alexander B. Gurvich ¹★, Jonathan Stern ², Claude-André Faucher-Giguère ¹, Philip F. Hopkins ³,
Andrew Wetzel ⁴, Jorge Moreno ^{3,5,6}, Christopher C. Hayward ⁷, Alexander J. Richings ⁸
and Zachary Hafen ⁶

¹Department of Physics & Astronomy and CIERA, Northwestern University, 1800 Sherman Ave, Evanston, IL 60201, USA

²School of Physics & Astronomy, Tel Aviv University, Tel Aviv 69978, Israel

³TAPIR, Mailcode 350-17, California Institute of Technology, Pasadena, CA 91125, USA

⁴Department of Physics & Astronomy, University of California, Davis, CA 95616, USA

⁵Department of Physics and Astronomy, Pomona College, Claremont, CA, USA

⁶Department of Physics & Astronomy, 4129 Reines Hall, University of California, Irvine, CA 92697, USA

⁷Center for Computational Astrophysics, Flatiron Institute, 162 5th Ave, New York, NY 10010, USA

⁸Institute for Computational Cosmology, Department of Physics, Durham University, South Road, Durham DH1 3LE, UK

Accepted 2022 December 13. Received 2022 December 13; in original form 2022 March 8

ABSTRACT

Recent observations and simulations indicate substantial evolution in the properties of galaxies with time, wherein rotationally supported and steady thin discs (like those frequently observed in the local Universe) emerge from galaxies that are clumpy, irregular, and have bursty star formation rates (SFRs). To better understand the progenitors of local disc galaxies, we carry out an analysis of three FIRE-2 simulated galaxies with a mass similar to the Milky Way at redshift $z = 0$. We show that all three galaxies transition from bursty to steady SFRs at a redshift between $z = 0.5$ and $z = 0.8$, and that this transition coincides with the rapid ($\lesssim 1$ Gyr) emergence of a rotationally supported interstellar medium (ISM). In the late phase with steady SFR, the rotational energy comprises $\gtrsim 90$ per cent of the total kinetic + thermal energy in the ISM, and is roughly half the gravitational energy. By contrast, during the early bursty phase, the ISM initially has a quasi-spheroidal morphology and its energetics are dominated by quasi-isotropic in- and outflows out of virial equilibrium. The subdominance of rotational support and out-of-equilibrium conditions at early times challenge the application of standard equilibrium disc models to high-redshift progenitors of Milky Way-like galaxies. We further find that the formation of a rotationally-supported ISM coincides with the onset of a thermal pressure supported inner circumgalactic medium (CGM). Before this transition, there is no clear boundary between the ISM and the inner CGM.

Key words: galaxies: disc – galaxies: evolution – galaxies: formation – galaxies: ISM – galaxies: star formation.

1 INTRODUCTION

Deep surveys of star-forming galaxies (SFGs) in the last 10–15 yr have revealed substantial evolution in their morphologies and kinematics with mass and time (see Förster Schreiber & Wuyts 2020 for a recent review). SFGs at redshifts $z \gtrsim 1$ are typically observed to have clumpy and/or disturbed morphologies in rest-UV light, which traces recent star formation (e.g. Elmegreen et al. 2007; Law et al. 2012; Guo et al. 2015), in contrast with the thin and regular star-forming discs commonly observed in the local Universe. Observations of ionized gas kinematics in high-redshift SFGs also often find that the rotational velocity V_{rot} is comparable or subdominant to a disordered velocity component with dispersion σ_g , suggesting that typical local discs ‘settle’ from disordered progenitors at $z \lesssim 1$ (Kassin et al. 2012; Simons et al. 2017). Despite the general decrease in importance of rotation with increasing lookback time, massive dynamically cold discs have been detected as early as $z \approx 4$ (Hodge et al. 2019;

Neeleman et al. 2020; Rizzo et al. 2020, 2021), and irregular star forming morphologies are common also at $z \sim 0$ at the low-mass end of the SFG population (e.g. Roberts 1969; Hunter 1997; Simons et al. 2015). These observations may indicate that mass, rather than redshift, is a primary determinant of whether a SFG is discy, while the trend with redshift is an indirect result of the growth of mass with time (Wisnioski et al. 2015; Harrison et al. 2017; Rodrigues et al. 2017; Tiley et al. 2019, 2021).

Another property of SFGs that appears to evolve with mass and cosmic time is the variability of the star formation rate (SFR). Star formation variability can be probed observationally by comparing SFRs inferred using indicators sensitive to different time-scales, such as $H\alpha$ which is sensitive to time-scales ~ 5 Myr versus far ultraviolet which is sensitive to ~ 10 – 100 Myr (e.g. Kennicutt & Evans 2012; Domínguez et al. 2015; Flores Velázquez et al. 2021). Using this approach several studies have reported evidence that dwarf galaxies have highly time-variable (‘bursty’) SFRs that can fluctuate by an order of magnitude or more on time-scales of 30–100 Myr, while more massive disc galaxies have more time-steady SFRs (Weisz et al. 2012; Kauffmann 2014; Sparre et al. 2017; Emami et al. 2019). It seems

* E-mail: agurvich@u.northwestern.edu

plausible that SF burstiness is connected to a disordered morphology (i.e. a lack of a stable rotating disc) at low mass or high redshift, either if a stable disc is a precondition for regulating star formation as in standard equilibrium disc models (e.g. Faucher-Giguère, Quataert & Hopkins 2013; Krumholz et al. 2018), or if enhanced stellar feedback from strong supernova clustering when star formation is bursty is able to disrupt the nascent disc (e.g. Martizzi 2020).

Analysing cosmological simulations that reproduce the observational trends mentioned above provides a promising route to understand the physical origin of these trends and the nature of bursty, dispersion-dominated SFGs at high-redshift and low mass. In the simulations one can infer properties such as the time-scale of the disc settling process, which are inaccessible to SFG population studies where only a single snapshot per galaxy is available.

In this paper, we analyse the physics of disc settling and its relation to the transition from bursty to steady star formation using cosmological zoom-in simulations from the FIRE project (Hopkins et al. 2014, 2018).¹ Similar to the trends suggested by observations, early low-mass FIRE galaxies have highly dynamic and clumpy gas morphologies (Hopkins et al. 2014; Ma et al. 2017), and during this phase the SFR is order-of-magnitude time variable (Sparre et al. 2017; Faucher-Giguère 2018; Flores Velázquez et al. 2021) while the corresponding bursty stellar feedback drives ‘gusty’ galactic winds (Muratov et al. 2015, 2017; Anglés-Alcázar et al. 2017; Pandya et al. 2021). At late times (or higher masses), the simulated galaxies develop a long-lived, thin disc similar to local spiral galaxies.

Previous physical explanations for the observed trends in SFGs typically fall within two broad categories. In the first category, some or all of these trends are attributed to a change in the properties of gaseous galaxy discs, such as an increase with redshift in the gas fraction of the disc, which makes the disc morphologically thicker and clumpier due to a larger Toomre mass (e.g. Dekel, Sari & Ceverino 2009; Krumholz et al. 2018). A challenge for these type of explanations is that they assume an equilibrium gas disc exists to begin with, a condition which is not clearly met at high redshift and low mass where many SFGs have $V_{\text{rot}} \lesssim \sigma_g$. A second category of explanations attributes observed SFG trends to a change in the rate or effect of mergers with mass and time (e.g. Brook et al. 2004; Bird et al. 2013; Dekel et al. 2020). It however remains to be seen if sufficiently massive mergers are common enough to cause such a large fraction of low-mass/high-redshift SFGs to appear disturbed.

There is also a third possibility, recently suggested by Stern et al. (2021a) and followed up by Yu et al. (2021) and Hafen et al. (2022), in which observed SFG trends correlate with a change in the physics of gas surrounding the galaxy, known as the circumgalactic medium (CGM). Due to the increase in gas cooling time in the CGM with mass, the CGM is expected to ‘virialize’ at a mass comparable to that in which discs are observed to settle, transitioning from a relatively cool and dynamic CGM at low masses to a hot and quasi-static CGM at high masses (White & Rees 1978; Birnboim & Dekel 2003; Kereš et al. 2005; Faucher-Giguère, Kereš & Ma 2011; Van de Voort & Schaye 2012; van de Voort et al. 2016; Fielding et al. 2017; Stern et al. 2020). This expected transition in the CGM has been shown to occur in the FIRE simulations at small halo radii, where cooling times are short relative to dynamical and cosmological time-scales (Stern et al. 2021a). CGM virialization affects both the physics of inflows on to the galaxy and the physics of galaxy outflows, and hence is likely to have significant effects on the properties of SFGs. In this work, we further demonstrate the connection between the

thermodynamics of the inner CGM and the properties of SFGs, by showing that the energetics of the ISM prior to disc settling in FIRE are similar to those in the inner CGM prior to virialization, while after the transition these two media are clearly separable. Hopkins et al. (in preparation) investigates the role of the gravitational potential, which is connected to CGM virialization, in the formation of disc galaxies.

Our analysis builds on Gurvich et al. (2020, hereafter G20), which focused on low-redshift, Milky Way-mass FIRE galaxies, well after discs have settled and when the SFRs have become steady. In that paper, we developed an analysis framework to quantify the different forms of ISM pressure in different thermodynamic phases. Here, we analyse the same three simulated galaxies as in G20, but now include the full evolution from early times to $z = 0$ using a modified version of the analysis framework that is applicable in both phases.

The outline of this paper is as follows. In Section 2, we summarize the simulations we analyse, define the coordinate frame and how we attribute gas resolution elements to the ISM or the CGM. In Section 3, we quantify the evolution of basic properties of the main galaxies, including the SFR, gas fraction, disc radius and thickness, and measures of rotational support. In Section 4, we extend the analysis of G20 to high-redshift using an analogous energy-based framework and quantify how energy in the ISM and inner CGM is partitioned between different forms of energy and thermodynamic phases, and how these results change over cosmic time. We discuss our results in Section 5 and summarize our main conclusions in Section 6.

2 SIMULATIONS AND ANALYSIS METHODS

2.1 Summary of simulations and their physics

We use FIRE-2 cosmological zoom-in simulations run with GIZMO, a publicly available gravity + magnetohydrodynamic code,² in its Meshless Finite Mass mode (Hopkins et al. 2018). MFM is a Lagrangian method that combines the advantages of traditional smooth particle hydrodynamics (SPH) and grid-based methods (for numerical details and tests, see Hopkins 2015). We provide a short summary of the relevant aspects here, while the full FIRE-2 physics model is described in Hopkins et al. (2018).

The simulations include radiative cooling for gas down to 10 K, including an approximate treatment of fine-structure metal and molecular lines. The gas is irradiated by a uniform, redshift-dependent ionizing background (Faucher-Giguère et al. 2009), as well as local sources. Star formation occurs in gas that is sufficiently dense ($n_{\text{H}} \geq 1000 \text{ cm}^{-3}$), self-gravitating, and self-shielding. When all criteria for star formation are satisfied, the gas particle is converted into a star particle representing a simple stellar population (that inherits its parent gas particle’s mass and metallicity) with 100 per cent efficiency per local free-fall time. A much lower star formation efficiency on galactic scales, and thus agreement with the observed Kennicutt–Schmidt relation, emerges as a result of regulation by stellar feedback (Hopkins et al. 2014; Orr et al. 2018).

The simulations include a multichannel model for stellar feedback. Star particles return mass, metals, momentum, and energy into the surrounding ISM, using rates that are functions of the star particle’s age following the STARBURST99 population synthesis model (Leitherer et al. 1999). These feedback processes include supernovae (Type II and Ia), stellar winds from O, B, and AGB stars, photoelectric heating, photoionization, and radiation pressure. The

¹See the FIRE project website: <http://fire.northwestern.edu>.

²Information about GIZMO and a public version of the code is available at: <https://www.tapir.caltech.edu/~phopkins/Site/GIZMO>.

model for radiation pressure includes both short-range and long-range components (Hopkins et al. 2020a).

In this paper, we focus on three representative Milky Way-mass galaxies from the FIRE project, which are chosen to match the sample analysed in G20: m12i, m12f, and m12b (see Wetzell et al. 2016; Garrison-Kimmel et al. 2017, 2019, for more details about these simulations). We note that the simulations were not selected to be perfect analogues of the Milky Way. For example, Sanderson et al. (2020) note the stellar velocity dispersions of these simulated galaxies at $z = 0$ are somewhat larger than in the Milky Way. We choose to focus on a relatively small number of runs compared to the entire FIRE catalogue in order to develop a new set of diagnostics that we intend to apply to the larger sample of FIRE galaxies, including at different mass scales, in future work. The runs we focus on in this paper are standard, hydrodynamic FIRE-2 simulations that include a subgrid model for turbulent metal diffusion but do not include the effects of magnetic fields or cosmic rays. The initial mass resolution in these simulations is $m_b \approx 7, 100 M_\odot$ for gas cells and star particles (evolved star particles can have up to 30 per cent lower mass owing to stellar mass loss). Thus, GMCs with masses $M_{\text{GMC}} \sim 10^6 - 10^7 M_\odot$ contain $\gtrsim 100 - 1000$ resolution elements. Gravitational softening lengths for gas cells are adaptive and reach values of ~ 5 pc at the average density of star-forming gas (see table 3 of Hopkins et al. 2018).

The simulated Milky Way mass galaxies all experience a transition from bursty to steady star formation, and form large, long-lived gas discs starting at redshifts $z < 1$ (Ma et al. 2017; Garrison-Kimmel et al. 2018). Fig. 1 shows gas temperature projections and mock Hubble renderings of the stellar distribution, generated using FIRE Studio, an open-source visualization software for cosmological simulations (Gurvich 2021). The images are centred on the main galaxies before and after disc settling. Star formation histories (SFHs) of the galaxies are shown in the bottom row. The $z = 0$ halo masses and stellar masses are catalogued in Table 1 for the simulations we analyse. We also list in the table the same quantities at the time when bursty star formation is identified to end, as discussed in Section 3.1.

In Appendix A, we present results for re-runs of m12i and m12b which include magnetic fields and cosmic-ray feedback from stars. These results indicate that our main conclusions for the ISM are not sensitive to the inclusion of these additional physics.

2.2 Galaxy tracking and coordinate system

As in G20, we use the Amiga Halo Finder (AHF; Gill, Knebe & Gibson 2004; Knollmann & Knebe 2009) to identify the peak mass density and virial radius R_{vir} of the main halo in each zoom-in simulation over cosmic time. The virial radius and virial halo mass are defined using the redshift-dependent overdensity criterion of Bryan & Norman (1998). At each snapshot, we define an analysis coordinate system such that the z -axis is parallel to the angular momentum of the stars within $5 R_{s,1/2}$, where $R_{s,1/2}$ is the 3D radius enclosing half of all the stellar mass within 20 per cent of R_{vir} . The origin of the coordinate system ($z = 0$) coincides with the halo centre as identified by AHF, and ϕ denotes the azimuthal angular coordinate. We define the orientation with respect to the stellar component rather than the gaseous component because at early times the gas orientation can rapidly change, whereas the stellar component evolves more smoothly. This produces a reference frame that changes between consecutive snapshots (time spacing ~ 20 Myr) on the order of $1 - 10$ deg during the bursty phase and typically a degree or less during the steady phase (Appendix B). The center-of-mass velocity is computed using the same stars that define the angular momentum vector.

2.3 Definition of ISM and inner CGM

We show below that at early times in our simulations gas at galaxy radii is not supported by rotation, and its geometry is quasi-spheroidal rather than disc like. Thus, in order to use a consistent definition of the ISM at all times (i.e. before and after the emergence of a stable galactic disc), we estimate for most figures ISM properties using mass-weighted averages on gas within a spherical radius $r < 0.05 R_{\text{vir}}$. Our main conclusions below are unchanged if instead we define the ISM using a quasi-cylindrical volume as in G20, where the ISM is defined as gas within a radial-dependent disc height $|z| < h(R)$. The similarity of the spherical and cylindrical cuts follows from the fact that at late times, when a disc has formed, the spherical averages are dominated by gas within the disc plane, while at early times $h(R) \sim R$.

The choice of maximum ISM radius $r = 0.05 R_{\text{vir}}$ is motivated by the expected radius of angular momentum support: gas with a spin parameter equal to the average value of dark matter haloes $\lambda = 0.035$ (e.g. Rodríguez-Puebla et al. 2016) will be angular momentum supported³ within $\sqrt{2}\lambda R_{\text{vir}} \approx 0.05 R_{\text{vir}}$. The gaseous discs which form at late times in our simulations indeed extend roughly out to this radius, supporting this choice (see below and fig. 13 in Stern et al. 2021a). The properties of the ‘inner CGM’ are estimated using mass-weighted averages of gas within a shell at $0.1 R_{\text{vir}}$ and with width of $0.01 R_{\text{vir}}$. The radius $0.1 R_{\text{vir}}$ is the smallest radius where angular momentum support does not significantly affect spherical averages at all times in our simulations, and can thus be considered ‘CGM’. The sensitivity of our conclusions to these radial choices is discussed below in Section 5.3.

3 BASIC PROPERTIES OF THE GALAXIES OVER COSMIC TIME

3.1 The transition from bursty to steady star formation

We measure the SFHs of each simulation using the ‘archaeological’ method, following the procedure outlined in Flores Velázquez et al. (2021). Put briefly, we take the stars within $5 R_{s,1/2}$ at redshift $z = 0$ and account for stellar mass-loss according to their ages and the rates from STARBURST99 (Leitherer et al. 1999). To construct an SFH, we group the stars according to their stellar formation times in bins spaced by 1 Myr. These SFHs are shown in the bottom row of Fig. 1 and in the top panel of Fig. 2, the latter normalized by a running mean within a 300 Myr window. The figure shows that the fluctuations from the mean SFR are large at early times (i.e. star formation is ‘bursty’) while at late times the fluctuations from the mean are much smaller (i.e. star formation is ‘steady’).

To quantify the fluctuations, we plot the running scatter in the (\log_{10} of the) SFH in 300 Myr windows,

$$\sigma_{300 \text{ Myr}}(\log(\text{SFR})) = \sqrt{\langle (\log(\text{SFR}))^2 \rangle_{300 \text{ Myr}} - \langle \log(\text{SFR}) \rangle_{300 \text{ Myr}}^2} \quad (1)$$

in the bottom panel of Fig. 2. We define t_{bursty} as the time after which $\sigma_{300 \text{ Myr}}$ remains below 0.3 dex (\approx a factor of 2). Our main results are not sensitive to the exact threshold used or exact size of the averaging window because $\sigma_{300 \text{ Myr}}$ drops rapidly by about a factor of five within a Gyr or less from t_{bursty} . We also considered two

³This follows from the spin parameter definition $j = \sqrt{2}\lambda R_{\text{vir}} v_{\text{vir}}$ (Bullock et al. 2001), so for a potential which is roughly isothermal we get $j = v_c r$ at $r = \sqrt{2}\lambda R_{\text{vir}}$.

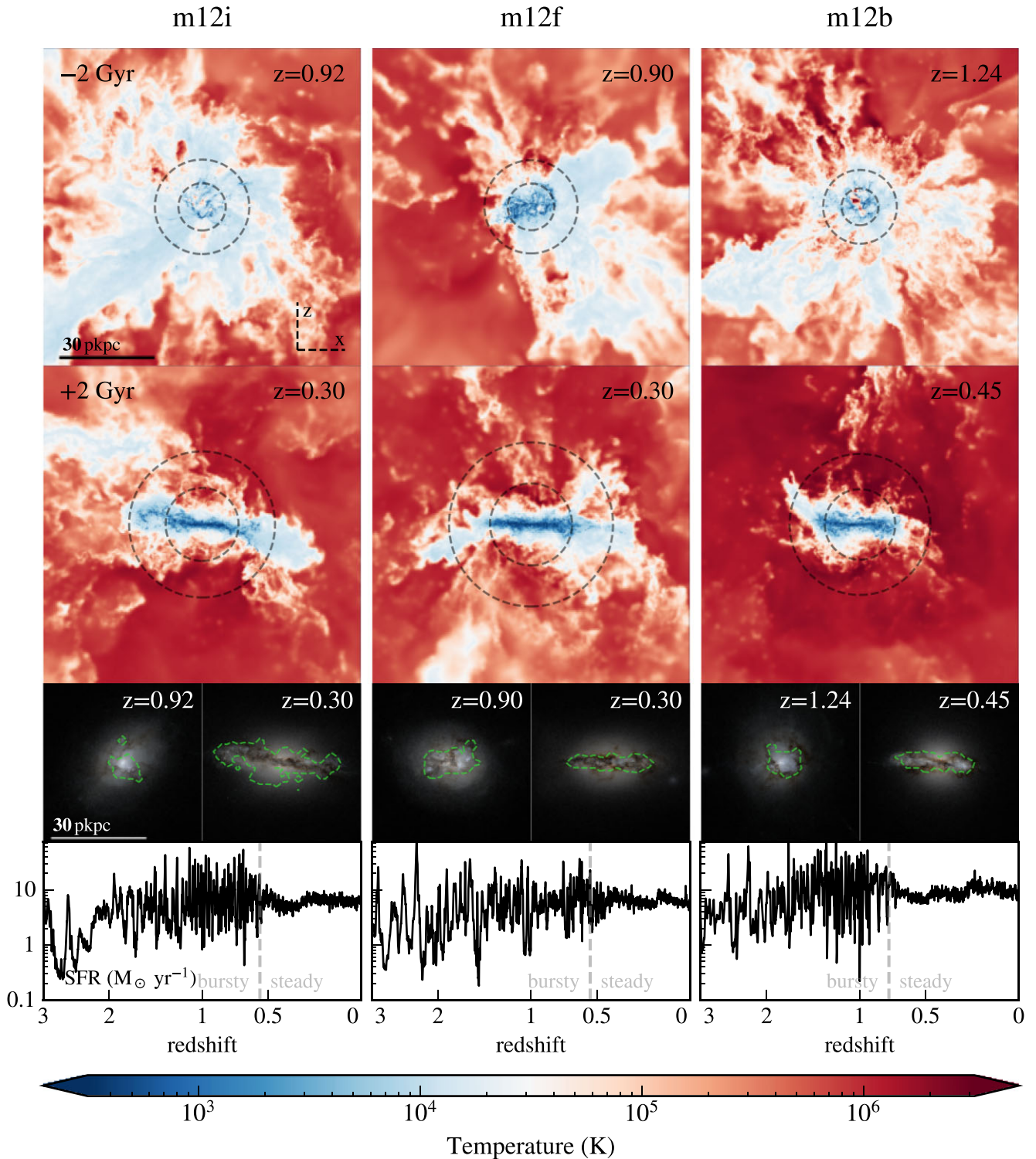


Figure 1. Edge-on gas temperature projections of three Milky Way-mass simulations, 2 Gyr before (top row) and 2 Gyr after (second row) they undergo a transition from bursty to time-steady SFRs. The projections include gas out to ± 10 kpc from the galaxy centre in the direction perpendicular to the page, and dashed circles mark $0.05R_{\text{vir}}$ and $0.1R_{\text{vir}}$, which we use to define regions corresponding to the ISM and inner CGM. For these projections, $\log T$ is weighted by mass along each line of sight. The third row shows mock Hubble renderings of simulated starlight for each of the two epochs. Green contours contain 99 per cent of stellar mass younger than 25 Myr and demonstrate the geometry of the star-forming region of the galaxy. The bottom row shows the SF history and the transition from bursty to steady star formation. Between the two epochs, the galaxy transforms from a clumpy, disturbed morphology with a bursty SFR, to a thin disc with a time-steady SFR. The temperature projections also show that during the bursty phase cold, warm, and hot gas mix at large radii ($\gtrsim 30$ kpc), whereas after the transition cold gas forms a disc embedded in a volume-filling hot galaxy atmosphere.

Table 1. Simulated galaxy properties.

Name	$z = 0$				$z = z_{\text{bursty}}$	
	M_{h}^a	M_{s}^b	t_{bursty}^c	z_{bursty}^c	M_{h}^a	M_{s}^b
m12i	1.18	6.36	8.34	0.56	0.81	3.41
m12f	1.62	6.78	8.41	0.55	1.07	3.41
m12b	1.30	9.80	7.11	0.76	0.76	3.69

Notes. ^aTotal mass (dark matter + baryon) within R_{vir} in units of $10^{12} M_{\odot}$.

^bTotal stellar mass within $5R_{\text{s},1/2}$ in units of $10^{10} M_{\odot}$.

^cCosmic time (in Gyr) and redshift of the transition from bursty to steady star formation.

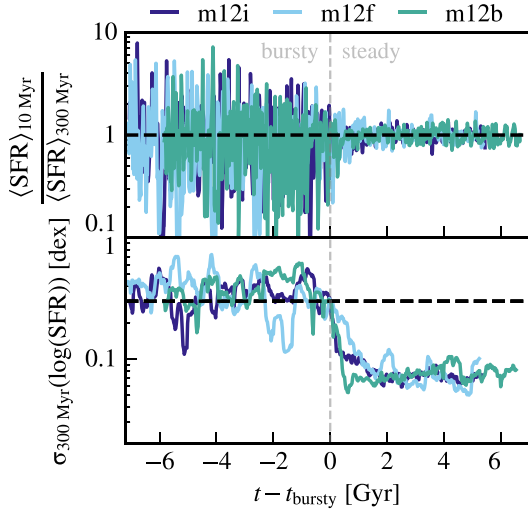


Figure 2. *Top:* The SFH of three Milky Way-mass simulations, normalized by the running average over 300 Myr and offset in time by the identified end of bursty star formation, t_{bursty} . *Bottom:* The running scatter of log SFR in 300 Myr windows. The transition epoch t_{bursty} is defined as the time after which this scatter stays below 0.3 dex. When offset by t_{bursty} , the three different simulations nearly overlap in both their normalized SFH and running SFH scatter.

additional definitions based on the peak-to-trough ratio in moving windows and the ratio of the running scatter to the running average in linear SFR as in Yu et al. (2021), and found variations in t_{bursty} of a few hundreds of Myr. This uncertainty in t_{bursty} is short relative to cosmological time-scales of 5–10 Gyr at the transition epoch. In Fig. 2 and following figures, we plot quantities as a function of $t - t_{\text{bursty}}$ rather than t , in order to highlight the correspondence between the transition from bursty to steady star formation, disc settling, and other changes in galaxy properties.

One could additionally define the power spectral distribution (PSD) of the SFR (as is done in e.g. Tacchella, Forbes & Caplar 2020) to measure the variation of the SFR on different time-scales, perhaps yielding a more generic definition of t_{bursty} . However, this does not appear warranted for the present analysis focused on three similar, Milky Way-mass galaxies. We defer such a PSD analysis of the SFR to future work.

3.2 Galaxy radii and gas fractions

In the top row of Fig. 3, we show the cylindrical half-mass radius for the gas, stars, and young stars (those with age ≤ 25 Myr) within $0.1R_{\text{vir}}$, smoothed with a moving 100 Myr window to improve readability. Before t_{bursty} , the young and total stellar populations are concentrated at relatively small radii of a few kpc. After t_{bursty} ,

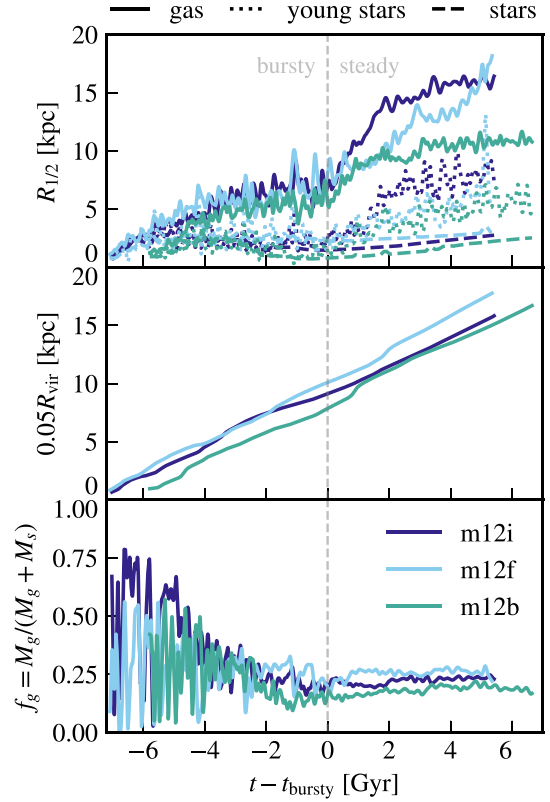


Figure 3. Properties of the galaxies in our sample as a function of cosmic time, offset by t_{bursty} (defined in the bottom panel of Fig. 2) and smoothed in a moving 100 Myr window for readability. *Top:* the cylindrical radius that encloses half of the mass in each of gas (solid), stars (dashed), and young stars (≤ 25 Myr old; dotted). During the bursty phase, the young and old stars have the same (relatively small) extent. In the steady phase, the young star and gas distributions become more extended. *Middle:* $0.05R_{\text{vir}}$, the size of the spherical region within which we measure properties of the ISM.

the gas distribution expands and active star formation extends to larger median radii of 5–10 kpc. The amount of star formation at these larger radii is however small compared to the integrated star formation during the bursty phase and as a result the half-mass radius of the total stellar population remains similar to that in the bursty phase.

The middle panel shows the evolution of a radius equal to $0.05R_{\text{vir}}$, within which we measure properties of the ISM (Section 2.3). The physical size corresponding to this definition increases over the course of the simulation, reaching ≈ 15 kpc at $z = 0$. Inner CGM properties are measured at $0.1R_{\text{vir}}$, corresponding to ≈ 30 kpc at $z = 0$.

In the bottom panel of Fig. 3 we plot the evolution of the baryonic gas mass fraction $f_g = M_g / (M_g + M_s)$ within a sphere of radius $0.05R_{\text{vir}}$, again smoothed using a moving 100 Myr window. The gas fraction is an important quantity in many equilibrium disc models, since the disc thickness and the characteristic mass of star-forming clumps (the Toomre mass) scale with the gas fractions (e.g. Thompson, Quataert & Murray 2005; Dekel et al. 2009; Faucher-Giguère et al. 2013; Hayward & Hopkins 2017; Faucher-Giguère 2018). The panel shows that the gas fraction decreases from large values ($f_g \gtrsim 50 - 60$ per cent) at high redshift to a more modest value of ≈ 20 per cent at $\sim t_{\text{bursty}}$, where the gas fractions plateau at values similar to local spiral galaxies (e.g. Leroy et al. 2008).

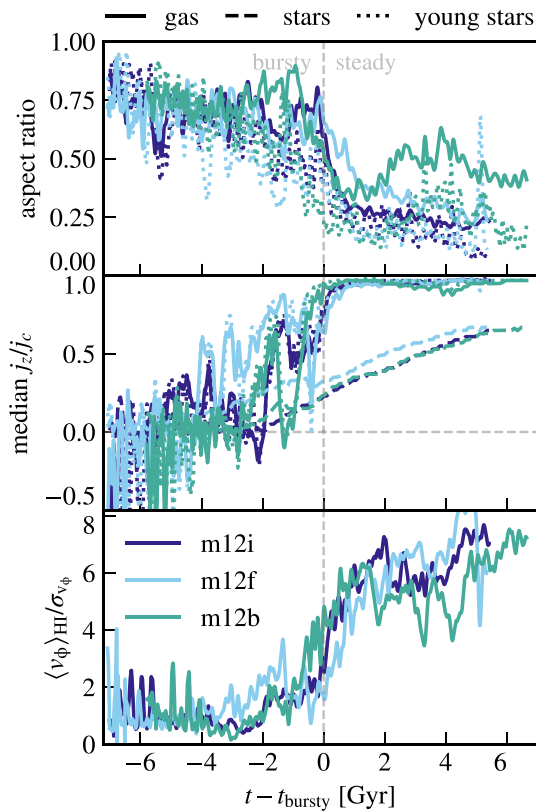


Figure 4. Three metrics of ‘disciness’ in our simulated galaxies versus cosmic time offset by t_{bursty} , and smoothed in a moving 100 Myr window for readability. *Top:* morphological axis aspect ratio (see Section 3.3 for definition), for young stars (dotted) and for gas within $0.1 R_{\text{vir}}$ (solid). *Middle:* The median circularity j_z/j_c , defined as the ratio of specific angular momentum in the z -direction to the specific angular momentum of gas in circular orbits, for gas within $0.05 R_{\text{vir}}$. *Bottom:* The ratio of the H I-weighted average of the rotational velocity to the H I-weighted dispersion in the rotational velocity (from Stern et al. 2021a).

Bottom: the baryonic gas fraction, $f_g = M_g/(M_g + M_s)$, within $0.05 R_{\text{vir}}$. Near the SFR transition the gas fraction settles on a value of ≈ 0.2 .

3.3 Geometric/kinematic metrics of disc settling

In order to understand the relation between the transition from bursty to steady star formation and disc settling, we analyse the evolution of multiple metrics of ‘disciness’ based on geometrical properties, kinematics, and angular momentum. Three such metrics of disciness are shown in Fig. 4, as a function of time relative to the identified transition from bursty to steady star formation, t_{bursty} . As for Fig. 3, we smooth the curves using a moving 100 Myr window for improved readability.

All panels suggest the appearance of a thin star-forming gaseous disc at $t \sim t_{\text{bursty}}$.

The top panel in Fig. 4 plots axis aspect ratios for the gas (solid) and for young stars within $0.1 R_{\text{vir}}$. For a quasi-spheroid, this ratio is expected to be ~ 1 , while it is expected to be $\lesssim 0.2$ for a thin disc similar to those in observed in the local Universe (e.g. Padilla & Strauss 2008). The axial ratio is measured by dividing the smallest principal axis with the mean of the two remaining principal axes, where the principal axes’ lengths are calculated from the eigenvectors and eigenvalues of the moment of inertia tensor. These eigenvectors

and eigenvalues define an ellipsoid approximating the orientation and extent of the mass distribution. This approach has the advantage of not relying on fitting a parametric model (e.g. an exponential profile or a cylindrical disc) which may not be applicable during the bursty phase. Hot gas with $T > 10^5$ K is excluded because it can trace the virialized CGM (if applicable) or thermalized outflows, rather than the ISM. The figure shows that at early times, the axis aspect ratio is 0.6–0.8 for both the young stars and the gas, indicating a geometry closer to spheroidal than disc like. At late times, the aspect ratios decrease to typically $\lesssim 0.3$, indicating a more disc-like geometry. Note that while the galactic discs in FIRE typically have a scale height that *increases* with increasing radius (like a ‘bowtie,’ see e.g. Gurvich et al. 2020), the ellipsoid from which principal axes are calculated has a different shape with an effective ‘height’ that *decreases* with increasing radius. Thus, since the minor axis of the ellipsoid must increase to compensate for the different shapes at large radii, the late-time aspect ratios are larger than may be expected for the ‘ h/R ’ ratio of a thin disc with a constant scale height (e.g. van der Kruit & Searle 1981), despite the high degree of rotational support at late times (see below). In future work, it would be interesting to address this mismatch more carefully and compare the ratios of individual principle axes to observed galaxy shapes.

In the middle panel of Fig. 4, we plot the median specific angular momentum in the z -direction (among resolution elements), j_z , normalized by the specific angular momentum of a circular orbit, $j_c \equiv v_c r$, for gas and stars within $0.05 R_{\text{vir}}$. The circular velocity v_c is calculated via $v_c = \sqrt{GM_{\text{enc}}(<r)/r}$, where $M_{\text{enc}}(<r)$ is the total enclosed mass within radius r .

The ratio j_z/j_c is bounded within the interval $[-1, 1]$, corresponding to a circular orbit that is aligned or anti-aligned with the orientation of the coordinate system. This ratio is sometimes referred to as the ‘circularity’, and circularities above 0.8 are interpreted as belonging to a ‘thin-disc’ (see for example Yu et al. 2021). For both the gas and young stars the median j_z/j_c increases from ≈ 0 with a large dispersion to uniformly ≈ 1 in the $\lesssim 2$ Gyr leading up to t_{bursty} , indicating the formation of a thin disc.

In the third panel of Fig. 4, we show the ratio of the rotational velocity to the velocity dispersion in the neutral gas from Stern et al. (2021a). Specifically, they compute the mean rotational velocity (in the ϕ -direction) weighted by H I mass, $\langle v_\phi \rangle_{\text{HI}}$, including all gas inside $0.05 R_{\text{vir}}$. They also compute the standard deviation of v_ϕ for the same gas, σ_{v_ϕ} , also weighted by HI mass, and the ratio $\langle v_\phi \rangle_{\text{HI}}/\sigma_{v_\phi}$. This kinematic ratio is useful because it is close to how the degree of rotational support is often estimated in observations (El-Badry et al. 2018). This metric as well shows a strong increase from ≈ 1 roughly two Gyr before t_{bursty} to values of ≈ 6 a Gyr after t_{bursty} .

All three metrics of disciness plotted in Fig. 4 indicate the emergence of a thin gas disc around t_{bursty} , with an increase in disciness appearing to begin 1–2 Gyr prior to t_{bursty} . These results highlight an important point for discussions of ‘disc settling.’ As best shown by the median j_z/j_c metric in the middle panel, what happens right around t_{bursty} is that nearly all the gas settles into nearly purely circular orbits, and the time fluctuations in circularity disappear almost entirely. Thus, we may say that t_{bursty} corresponds to the emergence of a steady (or stable), thin disc. However, despite the large fluctuations before t_{bursty} , substantial rotational support develops before the galaxy becomes steady. Therefore, observations that probe the instantaneous state of the gas would identify the ISM as discy during several time intervals prior to t_{bursty} . Moreover, the median circularity of the stellar distribution increases steadily before t_{bursty} , so observations of stars would find discy systems before t_{bursty} as well. In the papers by Yu et al. (2021, 2022), it is suggested that

the stars formed in the intermediate phase during which rotational support has become significant but the galaxy is still bursty could build up ‘thick’ discs.

In the next section, we examine the evolution of gas properties in more detail using energy-based metrics.

4 ENERGY-BASED METRICS OF DISC SETTLEMENT

We now present an energy-based analysis of how the gas evolves in the simulations, analogous to the pressure-based analysis in G20 for the same simulated galaxies in the late-time, steady phase. We analyse the energetics in radial shells rather than in cylindrical coordinates as in G20, due to the lack of a disc geometry prior to t_{bursty} (see Section 2.3).

4.1 Comparison of different forms of energy in the ISM

In this section we study how disc settling is expressed in the energetics of the ISM. To this end, for each snapshot we calculate the mass M , thermal energy E_{therm} , kinetic energy in each of the cylindrical coordinate velocity components, E_R , E_ϕ , and E_z , and gravitational potential energy E_{grav} for gas within $0.05R_{\text{vir}}$, i.e.

$$E_{j=R,\phi,z} = \frac{1}{2} \sum_i^{r < 0.05R_{\text{vir}}} m_i (v_i \cdot \hat{e}_j)^2,$$

$$E_{\text{grav}} = \sum_i^{r < 0.05R_{\text{vir}}} \frac{GM_{\text{enc}}(<r_i)m_i}{r_i^2}$$

$$E_{\text{kin}} = E_R + E_\phi + E_z$$

$$E_{\text{kin+therm}} = E_{\text{kin}} + E_{\text{therm}}, \quad (2)$$

where the sum over i is a sum over the resolution elements within a 3D radius $0.05R_{\text{vir}}$ and $M_{\text{enc}}(<r_i)$ is the total mass enclosed within the radius of the i th particle.

Gas denser than 50 cm^{-3} is excluded from the analysis, as it is primarily found in dense gravitationally bound clouds whose internal pressure decouples from the volume-filling medium. We verified that our results are not sensitive to the exact value of this cut.

Fig. 5 plots the ratios $E_\phi/E_{\text{kin+therm}}$ (top) and $E_{\text{kin+therm}}/E_{\text{grav}}$ (bottom) for the three simulations. As above, we smooth the curves using a 100 Myr moving window for improved readability. The figure shows that rotational support increases rapidly in the $\approx 1-2$ Gyr prior to t_{bursty} . After t_{bursty} , ISM energetics indicate a dynamically-cold rotating disc, with the rotational energy dominating over other kinetic (R and z) and thermal energy components, and equalling roughly half the gravitational potential energy, which is indicative of a type of virial equilibrium. At earlier times rotational energy is subdominant. Moreover, the total kinetic + thermal energy frequently exceeds the gravitational potential energy and the ratio experiences large fluctuations. These results suggest that at early times, the ISM is not well described as rotationally supported but rather much of the gas is gravitationally unbound and frequently ejected as bursty outflows (e.g. Muratov et al. 2015; Anglés-Alcázar et al. 2017). The system appears strongly out of equilibrium at these times.

Figs 6 and 7 further explore ISM energetics as a function of $t - t_{\text{bursty}}$, by plotting all kinetic and thermal components, and by partitioning the gas into different temperature phases: cold ($T < 10^3$ K, second panels from the left), warm ($10^3 < T < 10^5$ K, third panels) and hot ($T > 10^5$ K, right-most panels). We use m12b as an exemplar but the conclusions are valid also for m12i and m12f. The

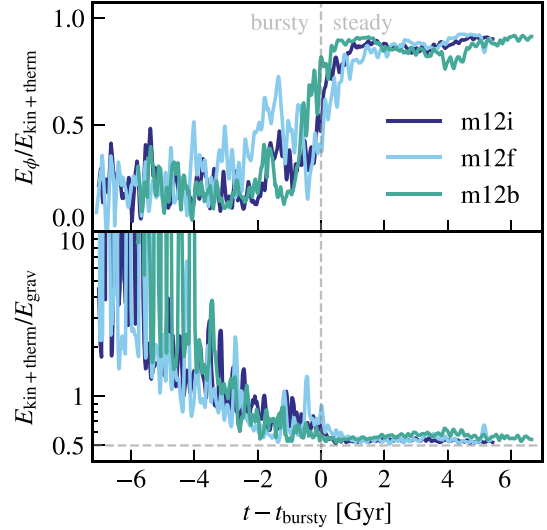


Figure 5. *Top:* Ratio of rotational energy to total kinetic + thermal energy in gas at $r < 0.05R_{\text{vir}}$, versus cosmic time offset by t_{bursty} for the three simulations. *Bottom:* The ratio of the total kinetic + thermal gas energy to the gravitational potential energy. The horizontal dashed line marks the ratio for a cold, rotationally supported disc. In all simulations, rotational support increases rapidly in the $\approx 1-2$ Gyr prior to t_{bursty} . After t_{bursty} , the energetics are strongly dominated by rotation and the large time fluctuations apparent before t_{bursty} have largely disappeared. While much of the gas is gravitationally unbound at early times, at late times the gas is consistent with being in a kind of virial equilibrium in the potential.

left-hand panel of Fig. 6 demonstrates that prior to t_{bursty} the thermal energy and different kinetic energy components are comparable, with rapid short-time-scale fluctuations. At $t \sim t_{\text{bursty}}$, the ISM becomes rotation-dominated (with rapid increase in rotational support in the preceding $\approx 1-2$ Gyr), as indicated by E_ϕ dominating other forms of energy. The three right-hand panels show that the kinetic energy originates in the cold and warm phases, and that also in these phases there is no strongly preferred orientation prior to t_{bursty} while rotation dominates after t_{bursty} . In the hot phase the total energy is dominated by thermal energy at all times, though its relative contribution to the total energy is small after t_{bursty} (see Section 4.2). One can also notice that in the hot phase E_ϕ increases relative to E_R and E_z at t_{bursty} , suggesting a similar split in kinetic energy as in the cold and warm phases.

The left-hand panel of Fig. 7 compares the different kinetic and thermal energy terms in m12b with E_{grav} . As suggested by Fig. 5, a dynamically cold disc with $E_\phi \approx E_{\text{grav}}/2$ and $E_R, E_z, E_{\text{therm}} \ll E_\phi$ is evident only after t_{bursty} . Before t_{bursty} the energy in the three kinetic components and the thermal component for all the gas are roughly equal and their sum exceeds $0.5E_{\text{grav}}$. The two middle panels show that the total kinetic + thermal energy in the cold and warm phases sums to $\approx 0.5E_{\text{grav}}$ also during the ≈ 3 Gyr prior to t_{bursty} . This suggests that a type of virial equilibrium is reached before t_{bursty} in these phases. This could be because while hot gas continues to be unbound as outflows, cold/warm clumps in the ISM become difficult to eject before the SFR stabilizes. At early times, the total kinetic + thermal energy frequently exceeds E_{grav} and experiences large fluctuations, suggesting out of equilibrium dynamics. In the hot phase (rightmost panel), the thermal energy exceeds E_{grav} at all times, indicating a thermally driven outflow (consistent with our previous findings at low redshift, see fig. 11 of G20), but by a larger factor before t_{bursty} indicating stronger winds during the bursty phase.

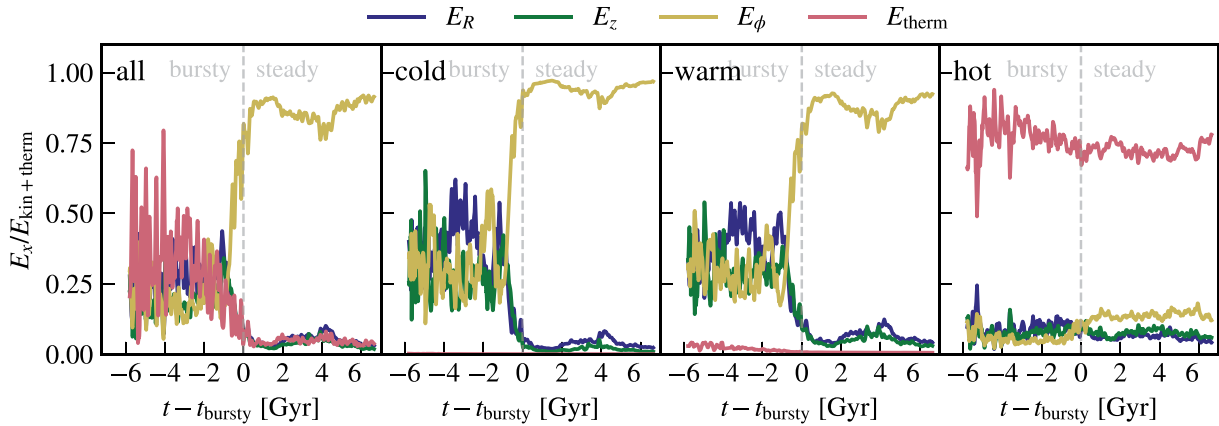


Figure 6. A partitioning of the total gas energy within $0.05R_{\text{vir}}$ versus cosmic time offset by t_{bursty} , for m12b. Different colours denote the thermal and three kinetic components (in cylindrical coordinates). The left-hand panel shows all gas, while the three right-hand panels focus on specific thermal phases: cold ($T < 1000$ K, second panel), warm ($1000 < T < 10^5$ K, third panel), and hot ($T > 10^5$ K, right-most panel). A strongly rotation-dominated ISM emerges only at $t \sim t_{\text{bursty}}$ (with rapid increase in rotational support in the preceding $\approx 1-2$ Gyr).

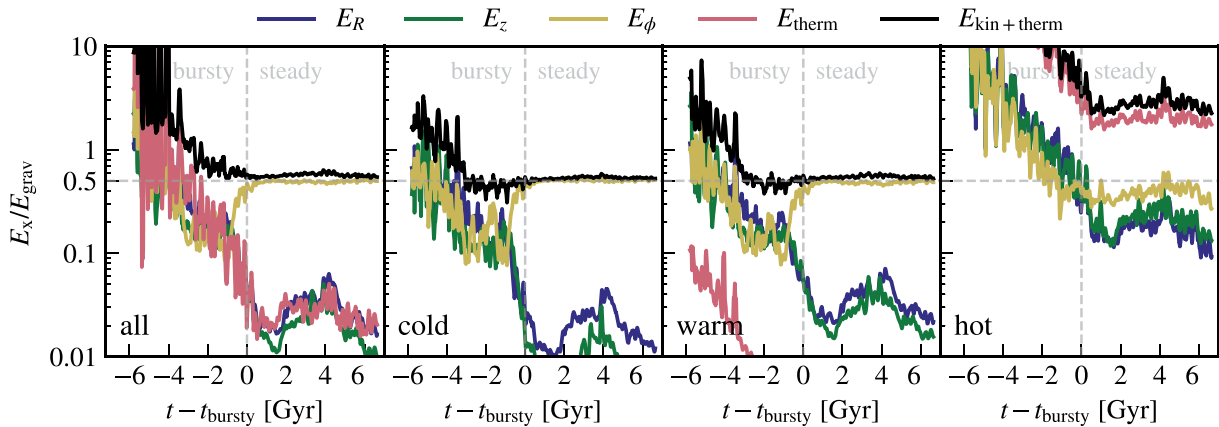


Figure 7. The ratio of different energy components to the gravitational potential energy, for gas within $0.05R_{\text{vir}}$ in m12b. The left-hand panel shows all gas while the three right-hand panels focus on gas in different gas temperature phases, as in Fig. 6. Rotational energy dominates after t_{bursty} and is then roughly equal to $0.5E_{\text{grav}}$, as expected for a rotationally supported cold disc. At early times, the total kinetic + thermal energy experiences large fluctuations and frequently exceeds the gravitational potential energy. This indicates that the galaxy is in a highly dynamical state and that the gas is out of equilibrium in the potential. The unbound gas reflects bursty outflows experienced by the galaxy at early times.

4.2 The relative importance of different temperature phases in the ISM

In this section we show the relative importance of the different temperature phases for the mass and energy of the ISM. The top panel of Fig. 8 plots the fraction of mass in each of the three different ISM temperature phases as a function of $t - t_{\text{bursty}}$, for m12b. As above we smooth the curves with a 100 Myr window for readability. The figure shows that the warm phase dominates the mass budget prior to t_{bursty} , with a subdominant but significant contribution from the cold phase and a typically small contribution from the hot phase. The fraction of cold gas substantially increases past t_{bursty} , becoming comparable to the warm phase, likely since higher densities and colder temperatures can be sustained after the ISM settles into a thin disc.

At earlier times the ISM energy is distributed roughly equally between the different kinetic and thermal components. The bottom panel in Fig. 8 plots the fraction of ISM energy in each temperature phase. The hot and warm phases dominate the energy budget before

t_{bursty} , with comparable contributions and large fluctuations. Around t_{bursty} both the contribution of the hot phase and the fluctuations substantially decrease, and the energy contribution from the cold phase becomes comparable to that of the warm phase. Fig. 8 thus supports the result from Figs 5–7 that the ISM energetics go through a transition at $t \approx t_{\text{bursty}}$.

4.3 Applying these metrics to the inner CGM

the ISM and inner CGM differ strongly in their distribution of energy components, with the ISM dominated by rotation and the inner CGM dominated by thermal energy.

Stern et al. (2021a) showed that the inner CGM in FIRE ‘virializes’ (i.e. becomes dominated by a steady, thermal-pressure-supported hot phase) when the halo mass exceeds $\sim 10^{12} M_{\odot}$. They also showed that this transition is associated with the transition from bursty star formation in the central galaxy and the settling of the gas into a stable, thin disc. In this section, we first explore the process of inner

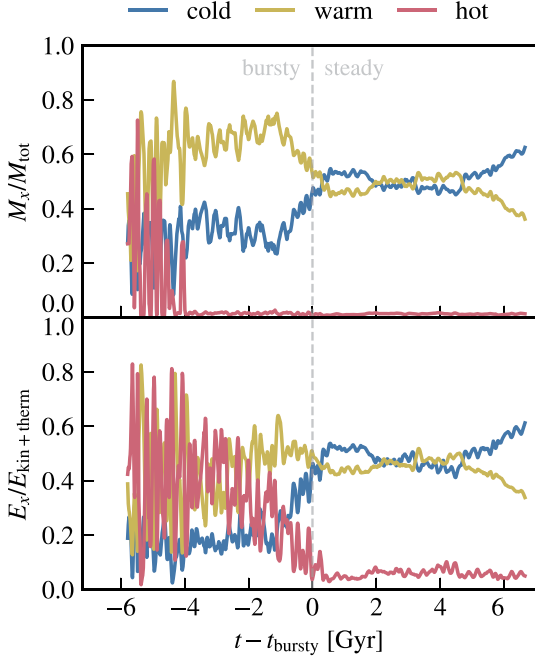


Figure 8. The fraction of mass (*top*) and energy (*bottom*) in each of the cold ($T < 1000$ K), warm ($1000 < T < 10^5$ K) and hot ($T > 10^5$ K) phases in the ISM of the m1.2b simulation. The mass and energy fractions of the cold gas increase starting $\approx 1-2$ Gyr before t_{bursty} , while the hot gas energy fraction and variability decrease.

CGM virialization with the same energy methodology employed above for the ISM, and then explore the connections between the transitions in the CGM and ISM.

Fig. 9 plots the mass and energy fractions of the different temperature phases in the inner CGM, similar to the ISM analysis in Fig. 8. The bottom panel shows that prior to t_{bursty} the energy in the hot phase is highly variable and roughly equal to the energy in the warm phase, while the top panel shows that the mass is dominated by the warm phase. In contrast, after t_{bursty} the hot phase dominates the energy and has a significant contribution to the mass, while the magnitude of the rapid fluctuations decreases. The contribution of the cold phase to the mass and energy is small in the CGM both before and after t_{bursty} . The top panel of Fig. 10 partitions the energy in the inner CGM into its kinetic and thermal components. Prior to t_{bursty} , most of the energy in the inner CGM is kinetic, while after t_{bursty} the thermal term is the largest, comprising more than half of the total energy. The bottom panel shows that the thermal energy is roughly equal to the gravitational energy after t_{bursty} indicating that the thermal energy is sufficient to support the gas against gravity. This transition, from an inner CGM dominated by kinetic motions to an inner CGM mostly supported by thermal pressure is the virialization of the inner CGM identified by somewhat different methods in Stern et al. (2021a).

In idealized CGM calculations, the CGM virializes when the cooling time of shocked hot gas $t_{\text{cool}}^{(s)}$ exceeds the free-fall time t_{ff} (e.g. White & Rees 1978; Birnboim & Dekel 2003; Fielding et al. 2017). Stern et al. (2020) used analytic calculations and idealized simulations to argue that this is true in a local sense, i.e. that the inner CGM just outside the galaxy virializes when the local value of $t_{\text{cool}}^{(s)}/t_{\text{ff}}$ exceeds unity, a result later shown to hold also in the FIRE simulations (Stern et al. 2021a). Here, we demonstrate this correspondence between $t_{\text{cool}}^{(s)}/t_{\text{ff}}$, virialization, and the end of bursty

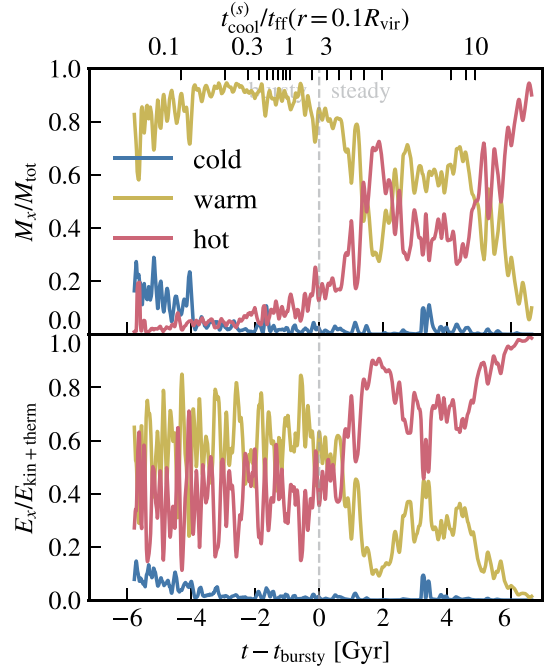


Figure 9. The fraction of mass (*top*) and energy (*bottom*) in each of the cold ($T < 1000$ K), warm ($1000 < T < 10^5$ K), and hot ($T > 10^5$ K) phases, in a thin shell at $r = 0.1R_{\text{vir}}$ corresponding to the inner region of the CGM, in the m1.2b simulation. After t_{bursty} , hot gas in the inner CGM dominates the energy and has a substantial contribution to the total mass. Prior to t_{bursty} , the hot CGM phase exhibits large short-time-scale variability, is comparable in energy to the warm phase, and negligible in mass. Comparison with Fig. 8 demonstrates that the mass and energy distributions in the inner CGM are qualitatively similar to those in the ISM prior to t_{bursty} , but differ strongly after t_{bursty} . The top axis denotes the ratio of the hot gas cooling time to the free-fall time of shocked gas. The hot CGM is expected to become dominant and steady when this ratio exceeds ~ 1 , consistent with the trend seen in the plot.

star formation by noting $t_{\text{cool}}^{(s)}/t_{\text{ff}}(0.1R_{\text{vir}})$ in the top axes of Figs 9 and 10. We calculate t_{ff} as (e.g. McCourt et al. 2012)

$$t_{\text{ff}} = \frac{\sqrt{2}r}{v_c}. \quad (3)$$

The value of $t_{\text{cool}}^{(s)}$ is calculated as

$$t_{\text{cool}}^{(s)} \equiv t_{\text{cool}}(T_c, P_{\text{HSE}}, Z, z), \quad (4)$$

where t_{cool} is the cooling time based on the Wiersma, Schaye & Smith (2009) tables, $T_c \equiv 0.6\mu m_p v_c^2(r)/k_B$ is comparable to the virial temperature, Z is the shell-averaged metallicity in the snapshot, and P_{HSE} is the pressure expected in hydrostatic equilibrium, i.e. it is equal to the weight of the overlying gas (equation 12 in Stern et al. 2021a). The value of $t_{\text{cool}}^{(s)}$ thus approximates the cooling time in a hot, thermal pressure-supported CGM, regardless of whether such a virialized CGM actually exists in the snapshot, and is thus analogous to the cooling time estimate used in the idealized calculations mentioned above. We refer the reader to Stern et al. (2021a, b) for a discussion of $t_{\text{cool}}^{(s)}$, how it evolves in the simulations as a function of mass and radius, and how it compares to other cooling time estimates. We note also that calculating $t_{\text{cool}}^{(s)}$ based on the average gas density in the shell rather than on P_{HSE} yields similar results.

Figs 9–10 demonstrate that the transitions in the CGM occur when $t_{\text{cool}}^{(s)}/t_{\text{ff}}$ exceeds ≈ 2 , consistent with the order unity value expected

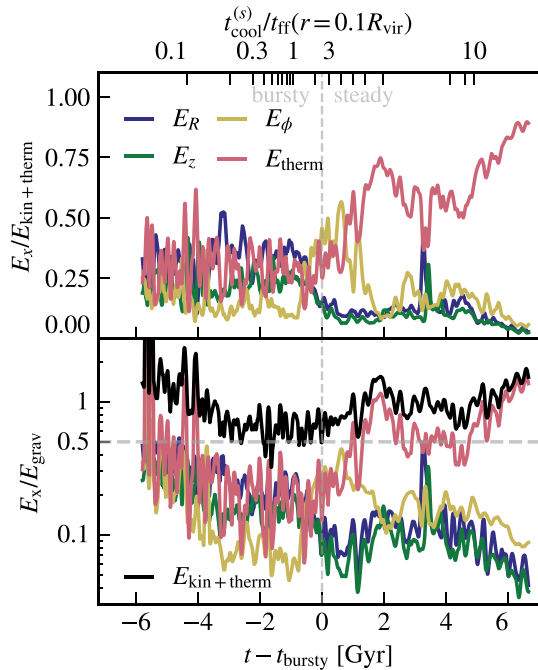


Figure 10. As Fig. 6, but for gas in a thin shell centred at $r = 0.1R_{\text{vir}}$ corresponding to the inner CGM. Different colors denote the thermal component and the three kinetic components, while the black line in the bottom panel denotes the total thermal and kinetic energy. The top axis denotes the ratio of the hot gas cooling time to the free-fall time of shocked gas. After t_{bursty} thermal energy dominates. Prior to t_{bursty} the inner CGM energy is split roughly equally between each of the kinetic components and the thermal energy, similar to the ISM prior to t_{bursty} (see Fig. 6). Only after t_{bursty} .

from the idealized calculations mentioned above, and with the range of $t_{\text{cool}}^{(s)}/t_{\text{ff}} \sim 1\text{--}4$ deduced in Stern et al. (2021a). This result also demonstrates that for the FIRE simulations we analyse, the time when $t_{\text{cool}}^{(s)}/t_{\text{ff}}$ exceeds unity and the inner CGM virializes are coincident with the epoch where star formation becomes steady and the ISM settles into a stable, thin disc. In Appendix C, we show that this correspondence between $t_{\text{cool}}^{(s)} \approx t_{\text{ff}}$ and $t \approx t_{\text{bursty}}$ applies to all three simulations analysed in this study. This relationship has been found to hold also in additional FIRE galaxies by Yu et al. (2021, see fig. 9 there).

5 DISCUSSION

In this paper, we use FIRE-2 cosmological zoom-in simulations to explore the properties of the ISM and inner CGM in MW-like galaxies versus time. We demonstrate that these FIRE galaxies experience two main, qualitatively distinct phases, separated by a transition period which is short ($\lesssim 1$ Gyr) relative to cosmological time-scales of $\sim 5\text{--}10$ Gyr at the transition epoch ($z \sim 0.5\text{--}0.8$). In the late phase, the SFR is steady, and the ISM forms a steady, rotation-dominated, thin disc (Fig. 4). During this phase rotational energy comprises > 90 per cent of the total kinetic and thermal energy in the ISM and equals half the gravitational energy, as expected in a dynamically cold, rotationally supported disc (Fig. 7). In contrast in the early phase, star formation is bursty (Fig. 2), the geometry is initially quasi-spheroidal, and ISM energetics are dominated by bulk flows (including both turbulence and coherent inflows/outflows) with no clear preference for rotation (Figs 5–6). While rotational

support starts building up $\approx 1\text{--}2$ Gyr before the formation of a steady, thin disc, the SFR is still bursty and the gas distribution is frequently disrupted; as mentioned above, this intermediate phase may be identified with the formation of a thick stellar disc (e.g. Yu et al. 2021, 2022). The ISM is on average hotter at the early times, with a smaller fraction of the ISM in the cold phase ($T < 10^3$ K) than in the late disc phase, and with a hot phase which is more dynamically important (Fig. 8). The ISM thus transitions from being supported against gravity by quasi-isotropic flows prior to t_{bursty} to being supported by rotation after $\sim t_{\text{bursty}}$. We further find that this transition in ISM properties is coincident with a transition in the inner CGM, from a medium dominated by kinetic energy (dispersion and bulk flows) to a medium dominated by thermal energy (Figs 9–10).

In this section, we discuss several implications of our results, and possible physical mechanisms that could be driving the transitions identified in the simulations.

5.1 A challenge for equilibrium disc models of high-redshift galaxies

In G20, we analysed the same simulated galaxies as in this work, focusing on their late-time properties, well after disc settling. In that study, we found that on average the total ISM pressure in the disc approximately balances the weight of the overlying gas (in the z -direction). This finding provided support for equilibrium disc models, which have been used to explain the origin of the Kennicutt–Schmidt relation as arising from a balance between stellar feedback and gravity in the disc (e.g. Thompson et al. 2005; Ostriker & Shetty 2011; Faucher-Giguère et al. 2013; Krumholz et al. 2018; Furlanetto 2021). In contrast, the results in this paper suggest that these equilibrium disc models do not apply to galaxies whose discs have not yet settled into a steady, thin configuration. In these equilibrium models, it is assumed that the ISM is well modelled by a rotationally supported disc, and that the vertical structure is determined by hydrostatic balance. In the limit in which the ISM pressure is dominated by gas turbulence with a velocity dispersion σ_g , the assumption of an equilibrium disc structure implies $\sigma_g \lesssim v_c$ ($\sigma_g \ll v_c$ for a thin disc), which in turn implies $E_{\text{kin} + \text{therm}} \lesssim E_{\text{grav}}$ and $E_\phi \approx 1/2 E_{\text{grav}}$. The results of Section 4.1 show that the assumptions stated above are not satisfied before t_{bursty} when considering all the gas. Rather, gas support is initially provided by quasi-isotropic bulk flows (including turbulence and coherent inflows and outflows powered by feedback and accretion). Besides these inequalities, the large fluctuations in energy ratios prior to t_{bursty} in Fig. 7 indicate departures from the usual equilibrium assumptions of standard equilibrium disc models. Moreover, values $E_{\text{kin} + \text{therm}} > E_{\text{grav}}$ imply that some of the gas is gravitationally unbound. While unbound gas is seen up until t_{bursty} , we note that when focusing on just the cold phase or just the warm phase, the simulation in Fig. 7 reaches $E_{\text{kin} + \text{therm}} \approx 1/2 E_{\text{grav}}$ well before t_{bursty} (by ~ 3 Gyr). This suggests that while hot outflows are unbound until t_{bursty} , most cold and warm gas becomes gravitationally bound earlier.

It is sometimes assumed that the ‘thick’ appearance of high-redshift galaxies can be explained by scaling relations derived for equilibrium discs supported by turbulence (e.g. $h/R \propto f_g$). Another common idea is that the massive bright ‘clumps’ observed in high-redshift galaxies correspond to a Toomre mass ($M_T \propto M_s f_g^3$), which is the characteristic mass for gravitational instability in discs (e.g. Dekel et al. 2009). These ideas have been useful to explain some properties of high-redshift galaxies found in observations and in simulations (e.g. Genzel et al. 2011; Oklopčić et al. 2017; Dekel

et al. 2022). While these scalings may be appropriate for massive high redshift galaxies whose discs have already settled into an equilibrium state (see Section 5.2 below), our analysis suggests that they do not accurately model the more common, lower-mass galaxies that do not yet have stable discs. Going forward, our decomposition of the total gas into different thermodynamic phases and forms of energy in the early bursty phase could be used as a starting point to develop more accurate and detailed ISM models for these early, lower-mass galaxies. Some recent studies have generalized equilibrium disc models to include oscillations around an equilibrium state, as may result from a time delay between star formation and stellar feedback (e.g. Orr et al. 2020; Furlanetto & Mirocha 2022). However, it is possible that some aspects would require a fully non-equilibrium approach.

Our discussion above focused on the implications of our results for equilibrium disc models, of the type that have been used to explain the Kennicutt–Schmidt relation. There is another class of ‘equilibrium’ models that have been widely used in galaxy formation, which are models in which the galactic SFR is determined by continuity arguments involving inflow and outflow rates (e.g. Bouché et al. 2010; Davé, Finlator & Oppenheimer 2012). These are also sometimes called ‘bathtub models.’ On sufficiently long time scales, our results do not invalidate this type of equilibrium models because a galaxy could have a highly time-variable SFR while on average satisfying the inflow–outflow continuity equations.

5.2 When and where do we expect discs?

In the analysis presented in this paper we focus on three simulations of Milky Way-mass galaxies, and show that they settle into thin discs on a \sim Gyr time-scale, concurrently with the onset of pressure support in the inner CGM (‘inner CGM virialization’). The previous analysis of Stern et al. (2021a) suggests that the correspondence between these transitions holds across a wide range of mass scales and redshifts, which allows us to extend the theoretical predictions to different mass scales. This is because the inner CGM is predicted to virialize at a halo mass $M_h \sim 10^{12} M_\odot$, roughly independent of redshift (Stern et al. 2020, 2021a, b). This predicts that halo mass, or equivalently the galaxy stellar mass given the weak evolution of the stellar mass–halo mass relation with redshift (Moster, Naab & White 2018; Behroozi et al. 2019), is a good proxy of whether a galaxy’s disc is expected to have settled. This implies that thin disc galaxies could exist at any redshift in sufficiently massive haloes, although thin discs will be relatively rare at high redshift due to the rarity of massive haloes. This picture is qualitatively consistent with the recent systematic analysis of integral field data by Tiley et al. (2021), which indicates that mass and not redshift is the primary variable determining the disciness of $z \sim 0$ –1.5 galaxies. Moreover, this would explain observations of rare large discs at higher redshifts, $z \gtrsim 4$ (e.g. Neeleman et al. 2020; Rizzo et al. 2020; Tsukui & Iguchi 2021).

The different transition times expected for galaxies with different growth histories can explain the apparent discrepancy between the rapidity of disc settling in our simulation versus the extended ‘epoch’ of disc settling at $z \sim 1$ identified in $M_* \sim 10^{10} M_\odot$ galaxy populations (e.g. Kassin et al. 2012). Indeed, even in our small sample of three Milky Way mass galaxies the transition time is spread out over $0.5 < z < 0.8$ (Table 1), and this period is further extended if more massive or lower mass galaxies are included in the sample. Thus, our results suggest that discs in individual galaxies settle rapidly relative to cosmological time-scales, but across galaxy populations discs forms over a cosmologically extended period.

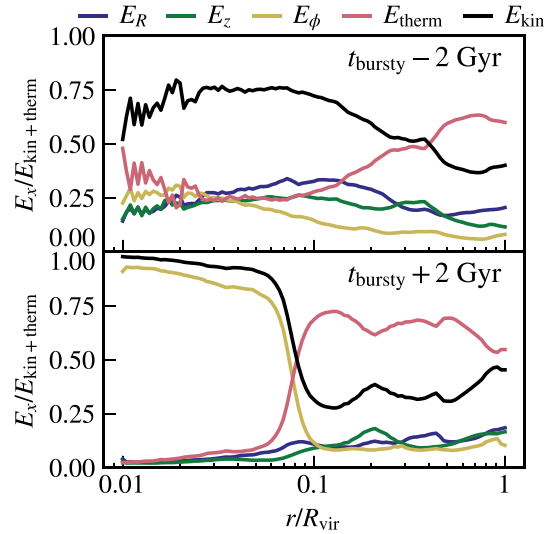


Figure 11. The contribution of different energy terms to the total kinetic + thermal energy versus radius, for two different times in the m12b simulation, 2 Gyr before t_{bursty} (top) and 2 Gyr after t_{bursty} (bottom). After t_{bursty} a clear transition is apparent between a rotation dominated ISM at $\leq 0.08 R_{\text{vir}}$ and a thermal energy dominated CGM at larger radii. In contrast, before t_{bursty} , kinetic energy dominates with no preference for rotation at both ISM and inner CGM radii, out to $\sim 0.3 R_{\text{vir}}$.

Our simulation results also appear qualitatively consistent with empirical results on the formation of the Milky Way. Recently, Belokurov & Kravtsov (2022) used abundance measurements from APOGEE and astrometry from *Gaia* and demonstrated that low-metallicity ($[\text{Fe}/\text{H}] \lesssim -1.3$) stars formed in situ (i.e. not accreted from other galaxies) have an approximately isotropic velocity ellipsoid and relatively little net rotation (see also Conroy et al. 2022 for related results from the H3 survey in combination with *Gaia* data). This stellar component, which they named ‘Aurora’, suggests an early phase of quasi-isotropic evolution in the Milky Way prior to disc formation, similar to our results. Belokurov & Kravtsov (2022) further show that the tangential velocity of the *in situ* stars, i.e. the degree of rotational support, increases sharply with metallicity between $[\text{Fe}/\text{H}] = -1.3$ and $[\text{Fe}/\text{H}] = -0.9$. Comparing their results with a set of simulations of Milky Way-mass galaxies, including publicly-available FIRE-2 simulations (Wetzel et al. 2022), they deduce a rapid disc ‘spin up’ time scale of ≈ 1 –2 Gyr. This conclusion is analogous to what our analysis predicts, though the Milky Way disc appears to form earlier and at lower metallicity than in the three simulations analysed in this paper. Belokurov & Kravtsov (2022) also note that disc spin up is accompanied by a qualitative change in chemical abundances (both in the observations and in the simulations), such that the scatter in abundances disappears around the time of disc spin up. They interpret the larger scatter in stellar abundances prior to disc formation as being likely caused by strongly time-variable inflow, outflow, and SFRs in the bursty phase. This is also consistent with our findings that before t_{bursty} our simulated galaxies are out of equilibrium and dominated by time-variable inflows and outflows.

5.3 Is there a distinction between the ISM and inner CGM?

The top row of Fig. 1 shows a complex morphology dominated by cool and warm gas extending to tens of kpc from the centre at 2 Gyr before t_{bursty} . In contrast, in the second row of this figure one

can clearly identify cool thin discs embedded in hot surroundings at 2 Gyr after t_{bursty} . This visual distinction (or lack thereof) is supported quantitatively by comparing Fig. 6 with Fig. 10, and is further explored in Fig. 11 where we plot the different energy terms versus radius at ± 2 Gyr from t_{bursty} . The plotted energy terms are calculated in spherical shells with thickness 0.01 dex spanning from 0.01 to $1R_{\text{vir}}$ in each snapshot and averaged over a time-span ± 300 Myr to avoid short time-scale fluctuations. After t_{bursty} (bottom panel), the distribution of energy shows a sharp transition at $\approx 0.08R_{\text{vir}}$, from being entirely dominated by rotation at smaller radii (i.e. the ISM), to being mostly thermal energy at larger radii (the CGM). In contrast, at the time before t_{bursty} shown in the top panel, kinetic energy dominates with $E_R \sim E_\phi \sim E_z$ at all radii out to $\approx 0.3-0.4R_{\text{vir}}$. The top panel thus demonstrates that both in the ISM and in the inner CGM velocity dispersion and bulk inflows/outflows provide most of the support against gravity prior to t_{bursty} , rather than rotation or thermal energy. Fig. 11 also demonstrates that this result is insensitive to the exact radius we use to attribute gas resolution elements to the ISM or inner CGM.

Figs 8–9 further demonstrate that before t_{bursty} the gas in both the ISM and inner CGM is dominated by the warm phase in terms of mass, while in terms of energy, both the ISM and the inner CGM have comparable contributions from the warm and hot phases. In contrast, after t_{bursty} the ISM is dominated by cold and warm phases while the inner CGM is hotter, dominated by the warm and hot phases. It is thus only after disc settling and the virialization of the inner CGM that the ‘standard picture’ for galaxy discs arises, in which a rotation-dominated, cool ISM is clearly distinct from a thermal pressure-dominated hot CGM. Prior to these transitions both the ISM and the inner CGM are dominated by kinetic energy with no preferred orientation, and there is no clear distinction between their energetics. The ISM and inner CGM form a single continuous medium supported by dispersion and bulk flows with intermediate temperatures. These two regimes are pictured schematically in Fig. 12.

The top panel of Fig. 11 shows that at large CGM radii ($>0.4R_{\text{vir}}$) thermal energy dominates also before the transition at $t = t_{\text{bursty}} - 2$ Gyr. Stern et al. (2021a, b) showed this is likely a result of $t_{\text{cool}}^{(s)}/t_{\text{ff}}$ increasing with radius and having values larger than unity in the outer CGM even when in the inner CGM this ratio is lower than unity and kinetic energy dominates. Our results thus suggest that after t_{bursty} when $t_{\text{cool}}^{(s)}/t_{\text{ff}} \gg 1$ at all radii, the distinction between the CGM and ISM is a result of rotational support, which is large in the ISM and small in the CGM. In contrast, prior to t_{bursty} the distinction between the outer CGM and the inner CGM/ISM is a result of cooling, which is rapid at small radii and slow at large radii. We note that the outer CGM also experiences a transition from being dominated by kinetic energy to being dominated by thermal energy, though at earlier times than this occurs in the inner CGM (fig. 12 in Stern et al. 2021a). At these very early times, we expect the entire ISM and CGM system to be dominated by kinetic energy.

5.4 What are the mechanisms that drive disc settling?

Above we find that at $t < t_{\text{bursty}}$ the ISM is supported against gravity by turbulence and coherent flows rather than by rotation (although there is evidence for build up of rotational support in the $\approx 1-2$ Gyr prior to t_{bursty} ; see Section 3.3). Given the rapid dissipation expected of such bulk flows (~ 100 Myr), the energy and momentum required to sustain them in our simulations is likely continuously supplied by

a combination of accretion energy and stellar feedback. It thus seems that the mechanism which drives disc settling is a mechanism that changes the effects of stellar feedback, from a relatively strong mode of feedback which dominates rotation and hence entirely disrupts the disc, to a weaker feedback mode which is subdominant to rotation and provides support primarily in the vertical direction, as in standard equilibrium disc models. Our results suggest that, for the Milky Way-mass galaxies we have analysed, this transition in the effects of stellar feedback occurs within a time-scale of \sim Gyr, as indicated by the transition time from $E_\phi/(E_{\text{kin}} + E_{\text{therm}}) \approx 0.2$ to $E_\phi/(E_{\text{kin}} + E_{\text{th}}) \approx 0.9$ in Figs 5–7. This transition time-scale is short compared to cosmological time-scales of ~ 10 Gyr, though it is long relative to galactic dynamical time-scales of ~ 100 Myr.

Previous studies have shown that galaxy-scale outflows subside in FIRE when the SFR becomes steady (Muratov et al. 2015; Anglés-Alcázar et al. 2017; Pandya et al. 2021). However, the physical mechanisms or properties driving these changes in SFR and feedback properties remain unclear. Previous studies based on idealized models and arguments suggested that a qualitative change in stellar feedback-driven outflows is expected when the disc crosses a threshold in the depth of its gravitational potential well (Dekel & Silk 1986), in its gas fraction (Hayward & Hopkins 2017; Fielding, Quataert & Martizzi 2018; Orr et al. 2020), in its dynamical time (Torrey et al. 2017; Faucher-Giguère 2018; Furlanetto & Mirocha 2022), or in its SFR surface density (Murray, Ménard & Thompson 2011; Kretschmer, Agertz & Teyssier 2020). All these quantities are correlated in our simulations, so it remains to be seen which of these suggested thresholds, if any, is the ultimate driver of the transitions. We note that many of these idealized arguments are based on analytic derivations that assume there is an equilibrium disc to begin with, a condition which is not met in our simulations at early times, so some of the thresholds derived may not apply as predicted.

The rough concurrence between t_{bursty} and the transition to a thermal pressure-supported inner CGM (Figs 9–10) and the similarity in the energetics of the ISM and inner CGM prior to t_{bursty} (Figs 11–12) suggest that the process of ‘inner CGM virialization’ may play an important role in disc settling, as proposed by Stern et al. (2021a). Inner CGM virialization causes accreted gas to have a narrow angular momentum distribution prior to accretion on to the central galaxy, due to more efficient angular momentum exchange in a thermal energy-dominated CGM, in contrast with a large dispersion in angular momentum in a cool CGM dominated by kinetic energy (Hafen et al. 2022). A thermal energy-dominated CGM is also more efficient in confining galactic outflows due to its uniform pressure, in contrast with large pressure fluctuations when kinetic energy dominates, which allow outflows to expand through paths of least resistance (Stern et al. 2021a).⁴ These transitions in accretion and feedback properties following inner CGM virialization would both be conducive to the formation of steady discs and a decrease in ISM velocity dispersion.

An important aspect of inner CGM virialization is that it can potentially explain in simple halo-based terms when, during their cosmological evolution, galaxies develop stable discs. This is because CGM virialization is expected to occur when $t_{\text{cool}}^{(s)}/t_{\text{ff}}$ exceeds unity,

⁴Some authors have previously suggested that stellar feedback-driven outflows may be suppressed after the CGM virializes because the outflows lose buoyancy when the halo becomes filled with hot gas (Bower et al. 2017; Keller, Kruijssen & Wadsley 2020). The effect mentioned here is different in that it focuses on the effects of pressure fluctuations in creating paths of least resistance in the CGM.

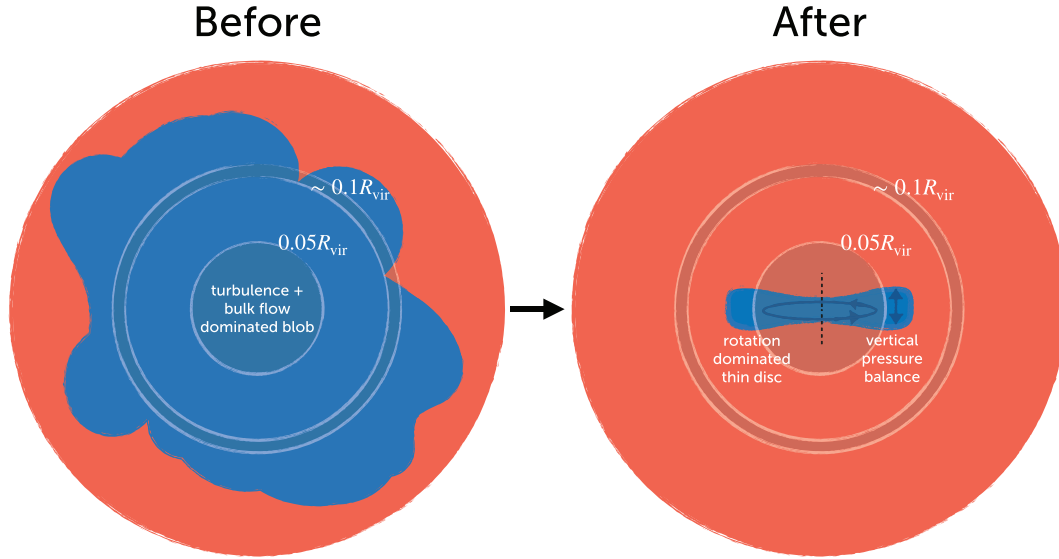


Figure 12. A schematic diagram of gas energetics before and after t_{bursty} , based on the quantitative results in Fig. 11 (not to scale). Red shows hot, virialized gas, and blue represents unvirialized gas (mostly cool, though warm/hot gas can be mixed in; see top row in Fig. 1). After t_{bursty} (right), there is a clear distinction between the rotationally supported ISM disc (with dispersion and bulk pressures supporting the disc vertically, see G20) and the hot, thermal pressure-supported CGM. In contrast, before t_{bursty} (left), there is a continuous medium dominated by turbulence and bulk in/outflows in all three directions, with no clear distinction between the energetics of the ISM and the inner CGM.

even when galactic outflows are neglected and insensitive to the detailed properties of the central galaxy. Indeed, a large number of cosmological simulations that neglected outflows and treated the ISM in subgrid found that gaseous haloes become hot when they reach a total mass $\sim \text{few} \times 10^{11} M_{\odot}$ (e.g. Kereš et al. 2005, 2009; Faucher-Giguère et al. 2011). As mentioned in Section 5.2, in reality the critical halo mass for virialization depends e.g. on gas metallicity, which is sensitive to feedback. However, for a range of well-motivated assumptions, analytic scalings and idealized models predict that the CGM should complete virialization within roughly ± 0.5 dex in halo mass from what is predicted neglecting feedback and metals (Birnboim & Dekel 2003; Stern et al. 2020), and this is indeed what is found in a larger sample of FIRE simulations that include realistic stellar feedback and metal enrichment (Stern et al. 2021a).

A potential alternative interpretation to the coincidence of inner CGM virialization and disc settling would be the reverse causality, i.e. that disc settling causes the inner CGM to virialize. If disc settling causes the outflows to be suppressed due to physical changes internal to the galaxy (e.g. if changes in the density PDF of the ISM make outflows less efficient at escaping through low-density channels; Hayward & Hopkins 2017), and the suppression of galactic outflows decreases gas densities and metallicities in the inner CGM, the cooling time of the CGM would increase thus pushing the gas toward a virialized state. We find this possibility unlikely, since suppression of outflows cause at most a factor of 2–3 changes in inner CGM density and metallicity, and hence also a similar change in $t_{\text{cool}}^{(s)}$, compared to a factor of ~ 1000 change in $t_{\text{cool}}^{(s)}$ as the halo grows in mass (Stern et al. 2021a, see especially fig. 2 there). Suppression of outflows following disc settling thus cannot, on its own, explain why disc settling occurs around the same halo mass scale as CGM virialization.

Another possibility is that inner CGM virialization and disc settling are coincident in time because both are correlated with a third variable. This is plausible because $t_{\text{cool}}^{(s)}/t_{\text{ff}}$ is a strong function of the gravitational potential depth, as quantified by the circular velocity v_c (see equation 17 in Stern et al. (2021a) and the discussion

in Byrne et al. submission) and Hopkins et al. (in preparation) present numerical evidence for the role of the potential in disc settling.

Finally, we note that even if CGM virialization is an important driver of disc settling, there could be mutually reinforcing effects involved. For instance, if inner CGM virialization initiates disc settling and contributes to suppressing outflows, then $t_{\text{cool}}^{(s)}/t_{\text{ff}}$ could increase for the reasons above, thus accelerating the virialization process. As a disc settles, its decreasing gas fraction and thickness (see Figs 3 and 4) bring down the Toomre mass $M_T \propto M_s f_g^3 \propto \Sigma_g h^2$. A smaller Toomre mass implies a larger number of lower mass star-forming regions distributed throughout the galaxy (as opposed to a small number of dominant clumps) and may reduce the disruptive effects of stellar feedback by limiting the clustering of supernovae. Mutually-reinforcing effects could help explain the rapidity of disc settling once the process starts.

Future work should attempt to more stringently test the causal links between inner CGM virialization and disc settling. Also, it would be worthwhile to investigate how the predictions for and mechanisms of disc settling depend on the subgrid models used in other cosmological simulations (e.g. Pillepich et al. 2019; Agertz et al. 2021; Bird et al. 2021; Park et al. 2021). For example, resolving the clustering of supernovae in the ISM is important for capturing SFR burstiness (e.g. Hu et al. 2022), and in FIRE the large fluctuations we find in several ISM and CGM properties before t_{bursty} are connected to SFR burstiness (see Section 4). These effects are likely to be suppressed in simulations that model the ISM using a smoother, effective equation of state for the ISM. Hu et al. (2022) also show that burstiness can be suppressed in adaptive mesh refinement codes that impose a minimum cell size, relative to Lagrangian codes, because such a minimum cell size reduces the clustering of star formation.

6 CONCLUSIONS

We analyse three FIRE-2 cosmological zoom-in simulations of Milky Way mass galaxies in order to characterize the properties

of their ISM and inner CGM before and after ‘disc settling.’ This analysis has implications for our theoretical understanding of the formation of disc galaxies, and may also be important to understand the disc settling phenomenon highlighted by recent morphological and kinematic observations of star-forming galaxies at a range of redshifts (e.g. Kassin et al. 2012; van der Wel et al. 2014; Simons et al. 2017; Tiley et al. 2021). We find the following:

(i) Milky Way-mass galaxies in the FIRE-2 simulations experience two phases of star formation: a dynamic ‘bursty’ phase of star formation at early times and a ‘time-steady’ phase of star formation at late times (Figs 1–2). The transition between the two regimes of star formation is rapid (< 1 Gyr) in each simulation, and occurs at $z \sim 0.5$ – 0.8 for galaxies in our sample. This transition between order-of-magnitude different levels of star formation variability is consistent with previous analyses of FIRE simulations (Muratov et al. 2015; Sparre et al. 2017; Faucher-Giguère 2018).

(ii) The transition from bursty to time-steady star formation is concurrent with the emergence of a stable, rotationally supported, thin gaseous disc (Figs 4–7). At early times, the ISM is instead supported against gravity by quasi-isotropic bulk flows, including turbulence and coherent inflows/outflows. Moreover, at early times the total thermal + kinetic energy in the gas frequently exceeds the gravitational binding energy by large factors. These results challenge the applicability of standard equilibrium disc models (e.g. Faucher-Giguère et al. 2013; Krumholz et al. 2018) to high-redshift galaxies prior to disc settling.

(iii) There is evidence that rotational support builds up in the ≈ 1 – 2 Gyr before the SFR stabilizes, although the gas distribution is frequently disrupted at these times. This intermediate phase may correspond to the formation of a thick stellar disc (Yu et al. 2021, 2022).

(iv) A quasi-isotropic ISM in the progenitors of Milky Way-like galaxies is consistent with the isotropic velocity distribution of low-metallicity stars formed *in situ* in the Milky Way (Belokurov & Kravtsov 2022; Conroy et al. 2022).

(v) The transition to a rotation-supported, geometrically thin ISM with steady star formation is concurrent with a transition to thermal pressure support at small CGM radii (‘inner CGM virialization’, Figs 9–10). This is consistent with results obtained by Stern et al. (2021a) for a larger set of simulations. Prior to disc settling, both the ISM and inner CGM are supported by bulk flows and there is no clear distinction between the ISM and the inner CGM, in contrast with after disc settling, following which angular momentum support provides a boundary. The coincidence between the formation of a steady, thin disc and inner CGM virialization raises the possibility that the process of CGM virialization plays a role in driving the settling of galactic discs.

There are several interesting directions for future work. In this paper, we have presented an in-depth analysis of disc settling in simulated Milky Way-mass galaxies. Going forward, it will be important to expand the analysis by applying the diagnostics developed herein to a larger sample of galaxies covering a wide range of halo mass. This would allow us to quantify to what extent disc settling proceeds in the same way for galaxies with different growth histories. It will also be valuable to produce observational predictions that can be directly compared with observations in order to assess whether the phenomenon of disc settling apparent in observations matches the evolution that we find in FIRE around the transition from bursty to steady star formation. Finally, there is more work to be done to disentangle causal links and more firmly establish the role of different physical factors, including inner CGM virialization, in driving the evolution of galaxy properties during disc settling.

Controlled numerical simulations, in which physical parameters such as galaxy properties versus CGM properties can be independently varied (as opposed to cosmological simulations in which various correlations are built in), could be very useful to clarify causality.

ACKNOWLEDGEMENTS

We thank Vasily Belokurov and Andrey Kravtsov for sharing an advance copy of their paper on the identification of the Aurora stellar component and its interpretation in terms of an early chaotic phase in the Milky Way’s evolution. We also thank the anonymous referee whose comments improved the quality of this manuscript. ABG was supported by an NSF-GRFP under grant DGE-1842165 and was additionally supported by NSF grants DGE-0948017 and DGE-145000. JS was supported by the Israel Science Foundation (grant no. 2584/21) and by the German Science Foundation via DIP grant STE 1869/2-1 GE625/17-1. CAFG was supported by NSF through grants AST-1715216, AST-2108230, and CAREER award AST-1652522; by NASA through grant 17-ATP17-0067; by STScI through grant HST-AR-16124.001-A; and by the Research Corporation for Science Advancement through a Cottrell Scholar Award. Support for PFH was provided by NSF Research Grants 1911233 & 20009234, NSF CAREER grant 1455342, NASA grants 80NSSC18K0562, HST-AR-15800.001-A. AW received support from: NSF grants CAREER 2045928 and 2107772; NASA ATP grants 80NSSC18K1097 and 80NSSC20K0513; HST grants AR-15809 and GO-15902 from STScI; a Scialog Award from the Heising-Simons Foundation; and a Hellman Fellowship. AJR was supported by a COFUND/Durham Junior Research Fellowship under EU grant 609412; and by the Science and Technology Facilities Council [ST/T000244/1]. Numerical calculations were run on the Caltech computer cluster Wheeler, the Northwestern computer cluster Quest, Frontera allocation FTA-Hopkins/AST20016 supported by the NSF and TACC, XSEDE allocations ACI-1548562, TG-AST140023, and TG-AST140064, and NASA HEC allocations SMD-16-7561, SMD-17-1204, and SMD-16-7592. ZH was supported by a Gary A. McCue postdoctoral fellowship at UC Irvine. The data used in this work were, in part, hosted on facilities supported by the Scientific Computing Core at the Flatiron Institute, a division of the Simons Foundation.

REFERENCES

- Agertz O. et al., 2021, *MNRAS*, 503, 5826
 Anglés-Alcázar D., Faucher-Giguère C.-A., Kereš D., Hopkins P. F., Quataert E., Murray N., 2017, *MNRAS*, 470, 4698
 Behroozi P., Wechsler R. H., Hearin A. P., Conroy C., 2019, *MNRAS*, 488, 3143
 Belokurov V., Kravtsov A., 2022, *MNRAS*, 514, 689
 Bird J. C., Kazantzidis S., Weinberg D. H., Guedes J., Callegari S., Mayer L., Madau P., 2013, *ApJ*, 773, 43
 Bird J. C., Loebman S. R., Weinberg D. H., Brooks A. M., Quinn T. R., Christensen C. R., 2021, *MNRAS*, 503, 1815
 Birnboim Y., Dekel A., 2003, *MNRAS*, 345, 349
 Bouché N. et al., 2010, *ApJ*, 718, 1001
 Bower R. G., Schaye J., Frenk C. S., Theuns T., Schaller M., Crain R. A., McAlpine S., 2017, *MNRAS*, 465, 32
 Brook C. B., Kawata D., Gibson B. K., Freeman K. C., 2004, *ApJ*, 612, 894
 Bryan G. L., Norman M. L., 1998, *ApJ*, 495, 80
 Bullock J. S., Dekel A., Kolatt T. S., Kravtsov A. V., Klypin A. A., Porciani C., Primack J. R., 2001, *ApJ*, 555, 240
 Chan T. K., Keres D., Gurvich A. B., Hopkins P., Trapp C., Ji S., Faucher-Giguère C.-A., 2022, *MNRAS*, 517, 597

- Conroy C. et al., 2022, preprint ([arXiv:2204.02989](https://arxiv.org/abs/2204.02989))
- Davé R., Finlator K., Oppenheimer B. D., 2012, *MNRAS*, 421, 98
- Dekel A., Silk J., 1986, *ApJ*, 303, 39
- Dekel A., Sari R., Ceverino D., 2009, *ApJ*, 703, 785
- Dekel A., Ginzburg O., Jiang F., Freundlich J., Lapiner S., Ceverino D., Primack J., 2020, *MNRAS*, 493, 4126
- Dekel A., Mandelker N., Bournaud F., Ceverino D., Guo Y., Primack J., 2022, *MNRAS*, 511, 316
- Domínguez A., Siana B., Brooks A. M., Christensen C. R., Bruzual G., Stark D. P., Alavi A., 2015, *MNRAS*, 451, 839
- El-Badry K. et al., 2018, *MNRAS*, 477, 1536
- Elmegreen D. M., Elmegreen B. G., Ravindranath S., Coe D. A., 2007, *ApJ*, 658, 763
- Emami N., Siana B., Weisz D. R., Johnson B. D., Ma X., El-Badry K., 2019, *ApJ*, 881, 71
- Faucher-Giguère C. A., 2018, *MNRAS*, 473, 3717
- Faucher-Giguère C.-A., Lidz A., Zaldarriaga M., Hernquist L., 2009, *ApJ*, 703, 1416
- Faucher-Giguère C.-A., Kereš D., Ma C. P., 2011, *MNRAS*, 417, 2982
- Faucher-Giguère C.-A., Quataert E., Hopkins P. F., 2013, *MNRAS*, 433, 1970
- Fielding D., Quataert E., Martizzi D., Faucher-Giguère C.-A., 2017, *MNRAS*, 470, L39
- Fielding D., Quataert E., Martizzi D., 2018, *MNRAS*, 481, 3325
- Flores Velázquez J. A. et al., 2021, *MNRAS*, 501, 4812
- Förster Schreiber N. M., Wuyts S., 2020, *ARA&A*, 58, 661
- Furlanetto S. R., 2021, *MNRAS*, 500, 3394
- Furlanetto S. R., Mirocha J., 2022, *MNRAS*, 511, 3895
- Garrison-Kimmel S. et al., 2017, *MNRAS*, 471, 1709
- Garrison-Kimmel S. et al., 2018, *MNRAS*, 481, 4133
- Garrison-Kimmel S. et al., 2019, *MNRAS*, 487, 1380
- Genzel R. et al., 2011, *ApJ*, 733, 101
- Gill S. P. D., Knebe A., Gibson B. K., 2004, *MNRAS*, 351, 399
- Guo Y. et al., 2015, *ApJ*, 800, 39
- Gurvich A. B., 2021, Astrophysics Source Code Library, record ascl:2202.006
- Gurvich A. B. et al., 2020, *MNRAS*, 498, 3664 (G20)
- Hafen Z. et al., 2022, *MNRAS*, 514, 5056
- Harrison C. M. et al., 2017, *MNRAS*, 467, 1965
- Hayward C. C., Hopkins P. F., 2017, *MNRAS*, 465, 1682
- Hodge J. A. et al., 2019, *ApJ*, 876, 130
- Hopkins P. F., 2015, *MNRAS*, 450, 53
- Hopkins P. F., Kereš D., Oñorbe J., Faucher-Giguère C.-A., Quataert E., Murray N., Bullock J. S., 2014, *MNRAS*, 445, 581
- Hopkins P. F. et al., 2018, *MNRAS*, 480, 800
- Hopkins P. F., Grudić M. Y., Wetzel A., Kereš D., Faucher-Giguère C.-A., Ma X., Murray N., Butcher N., 2020a, *MNRAS*, 491, 3702
- Hopkins P. F. et al., 2020b, *MNRAS*, 492, 3465
- Hu C.-Y. et al., 2022, preprint ([arXiv:2208.10528](https://arxiv.org/abs/2208.10528))
- Hunter D., 1997, *PASP*, 109, 937
- Kassin S. A. et al., 2012, *ApJ*, 758, 106
- Kauffmann G., 2014, *MNRAS*, 441, 2717
- Keller B. W., Kruijssen J. M. D., Wadsley J. W., 2020, *MNRAS*, 493, 2149
- Kennicutt Jr. R. C., Evans N. J., 2012, *ARA&A*, 50, 531
- Kereš D., Katz N., Weinberg D. H., Davé R., 2005, *MNRAS*, 363, 2
- Kereš D., Katz N., Fardal M., Davé R., Weinberg D. H., 2009, *MNRAS*, 395, 160
- Knollmann S. R., Knebe A., 2009, *ApJ*, 182, 608
- Kretschmer M., Agertz O., Teyssier R., 2020, *MNRAS*, 497, 4346
- Krumholz M. R., Burkhardt B., Forbes J. C., Crocker R. M., 2018, *MNRAS*, 477, 2716
- Law D. R., Steidel C. C., Shapley A. E., Nagy S. R., Reddy N. A., Erb D. K., 2012, *ApJ*, 745, 85
- Leitherer C. et al., 1999, *ApJ*, 123, 3
- Leroy A. K., Walter F., Brinks E., Bigiel F., de Blok W. J. G., Madore B., Thornley M. D., 2008, *AJ*, 136, 2782
- Ma X., Hopkins P. F., Wetzel A. R., Kirby E. N., Anglés-Alcázar D., Faucher-Giguère C.-A., Kereš D., Quataert E., 2017, *MNRAS*, 467, 2430
- Martizzi D., 2020, *MNRAS*, 492, 79
- McCourt M., Sharma P., Quataert E., Parrish I. J., 2012, *MNRAS*, 419, 3319
- Moster B. P., Naab T., White S. D. M., 2018, *MNRAS*, 477, 1822
- Muratov A. L., Kereš D., Faucher-Giguère C.-A., Hopkins P. F., Quataert E., Murray N., 2015, *MNRAS*, 454, 2691
- Muratov A. L. et al., 2017, *MNRAS*, 468, 4170
- Murray N., Ménard B., Thompson T. A., 2011, *ApJ*, 735, 66
- Neeleman M., Prochaska J. X., Kanekar N., Rafelski M., 2020, *Nature*, 581, 269
- Oklopčić A., Hopkins P. F., Feldmann R., Kereš D., Faucher-Giguère C.-A., Murray N., 2017, *MNRAS*, 465, 952
- Orr M. E. et al., 2018, *MNRAS*, 478, 3653
- Orr M. E. et al., 2020, *MNRAS*, 496, 1620
- Ostriker E. C., Shetty R., 2011, *ApJ*, 731, 41
- Padilla N. D., Strauss M. A., 2008, *MNRAS*, 388, 1321
- Pandya V. et al., 2021, *MNRAS*, 508, 2979
- Park M. J. et al., 2021, *ApJS*, 254, 2
- Pillepich A. et al., 2019, *MNRAS*, 490, 3196
- Rizzo F., Vegetti S., Powell D., Fraternali F., McKean J. P., Stacey H. R., White S. D. M., 2020, *Nature*, 584, 201
- Rizzo F., Vegetti S., Fraternali F., Stacey H. R., Powell D., 2021, *MNRAS*, 507, 3952
- Roberts M. S., 1969, *AJ*, 74, 859
- Rodrigues M., Hammer F., Flores H., Puech M., Athanassoula E., 2017, *MNRAS*, 465, 1157
- Rodríguez-Puebla A., Behroozi P., Primack J., Klypin A., Lee C., Hellinger D., 2016, *MNRAS*, 462, 893
- Sanderson R. E. et al., 2020, *ApJS*, 246, 6
- Simons R. C., Kassin S. A., Weiner B. J., Heckman T. M., Lee J. C., Lotz J. M., Peth M., Tchernyshyov K., 2015, *MNRAS*, 452, 986
- Simons R. C. et al., 2017, *ApJ*, 843, 46
- Sparre M., Hayward C. C., Feldmann R., Faucher-Giguère C.-A., Muratov A. L., Kereš D., Hopkins P. F., 2017, *MNRAS*, 466, 88
- Stern J., Fielding D., Faucher-Giguère C.-A., Quataert E., 2020, *MNRAS*, 492, 6042
- Stern J. et al., 2021a, *ApJ*, 911, 88
- Stern J. et al., 2021b, *MNRAS*, 507, 2869
- Tacchella S., Forbes J. C., Caplar N., 2020, *MNRAS*, 497, 698
- Thompson T. A., Quataert E., Murray N., 2005, *ApJ*, 630, 167
- Tiley A. L. et al., 2019, *MNRAS*, 482, 2166
- Tiley A. L. et al., 2021, *MNRAS*, 506, 323
- Torrey P., Hopkins P. F., Faucher-Giguère C.-A., Vogelsberger M., Quataert E., Kereš D., Murray N., 2017, *MNRAS*, 467, 2301
- Tsukui T., Iguchi S., 2021, *Science*, 372, 1201
- Van de Voort F., Schaye J., 2012, *MNRAS*, 423, 2991
- van de Voort F., Quataert E., Hopkins P. F., Faucher-Giguère C.-A., Feldmann R., Kereš D., Chan T. K., Hafen Z., 2016, *MNRAS*, 463, 4533
- van der Kruit P. C., Searle L., 1981, *A&A*, 95, 105
- van der Wel A. et al., 2014, *ApJ*, 792, L6
- Weisz D. R. et al., 2012, *ApJ*, 744, 44
- Wetzel A. R., Hopkins P. F., Kim J.-h., Faucher-Giguère C.-A., Kereš D., Quataert E., 2016, *ApJ*, 827, L23
- Wetzel A. et al., 2022, preprint ([arXiv:2202.06969](https://arxiv.org/abs/2202.06969))
- White S. D. M., Rees M. J., 1978, *MNRAS*, 183, 341
- Wiersma R. P. C., Schaye J., Smith B. D., 2009, *MNRAS*, 393, 99
- Wisnioski E. et al., 2015, *ApJ*, 799, 209
- Yu S. et al., 2021, *MNRAS*, 505, 889
- Yu S. et al., 2022, preprint ([arXiv:2210.03845](https://arxiv.org/abs/2210.03845))

APPENDIX A: THE EFFECTS OF MAGNETIC FIELDS AND COSMIC RAYS

Fig. A1 demonstrates the dependence of some of our results on the inclusion magnetohydrodynamics (MHD) and cosmic rays in our simulations, focusing the `m12i` and `m12i` runs, for which we have variants with and without these physics included. The runs with MHD also include anisotropic thermal conduction and viscosity, while the

runs with CRs include all these physics plus anisotropic diffusion and streaming of cosmic rays with an effective diffusion coefficient $\kappa = 3 \times 10^{29} \text{ cm}^2 \text{ s}^{-1}$. These runs are labeled ‘MHD+’ and ‘CR +’ in previous papers that introduced them and analysed them in more detail (e.g. Hopkins et al. 2020b; Chan et al. 2022).

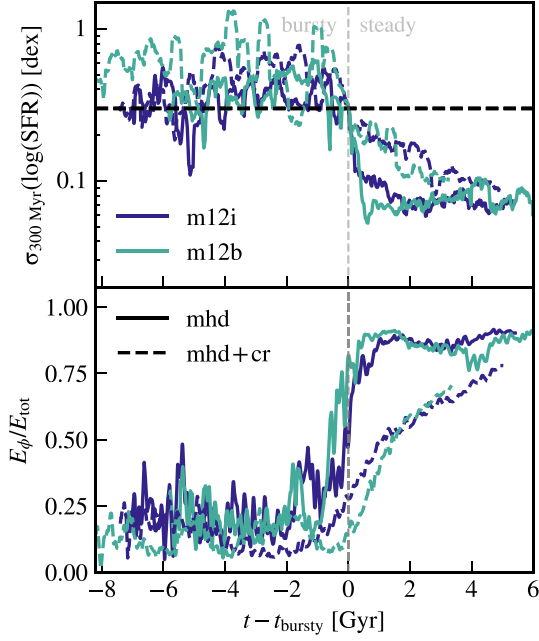


Figure A1. Comparison of our core results for two simulations with identical initial conditions, which include magnetic fields and either exclude (solid) or include (dashed) cosmic ray physics. Top panel shows the running scatter in the SFR in a 300 Myr moving window, similar to Fig. 2. The bottom panel shows the ratio of rotational energy to total kinetic and thermal energy, as in Fig. 5.

The top panel of Fig. A1 shows that there is a bursty SFR transition even when these physics are included. The bottom panel shows that the fraction of kinetic energy, in the ϕ -direction sharply increases at t_{bursty} in the MHD-only simulations as in the fiducial simulations analysed in the main text. A more gradual increase in the fraction of rotational energy is seen in the simulations which include cosmic rays. We defer exploring the effects of CRs in more detail to future work; these are most likely dependent on the (uncertain) assumptions adopted for cosmic-ray transport.

APPENDIX B: STABILITY OF THE COORDINATE FRAME

In this paper, we define the z -axis in each snapshot to be parallel to the total angular momentum vector of the stars within $0.2 R_{\text{vir}}$ (Section 2).

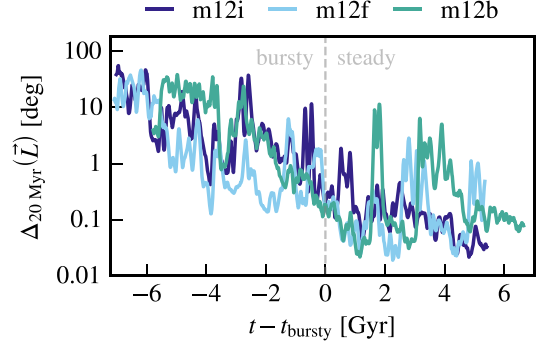


Figure B1. The change in the total stellar angular momentum vector within $0.2R_{\text{vir}}$ between consecutive 20 Myr time slices versus cosmic time offset by t_{bursty} . This vector is used to define the z -axis of the coordinate system for our analysis. At early times, in the bursty phase, the stellar angular momentum vector varies by $\sim 1\text{--}30$ deg between consecutive time slices. In the steady phase, after t_{bursty} , the change between consecutive time slices drops to typical values $\lesssim 1$ deg. Larger peaks are associated with galaxy interactions, such as mergers.

In this section, we test how the orientation of this coordinate system changes with time.

Snapshots in our simulation are unevenly separated by $\Delta t \sim 20\text{--}50$ Myr, so we resample the total angular momentum vector with a uniform spacing in time with a fixed $\Delta t = 20$ Myr by linear interpolation. Fig. B1 plots the angle between each of these consecutive angular momentum vectors,

$$\Delta_{20 \text{ Myr}}(\vec{L}) = \cos^{-1}(\vec{L}(t) \cdot \vec{L}(t + 20 \text{ Myr})), \quad (\text{B1})$$

as a function of time. The figure demonstrates that during the bursty phase, when the galaxy is out of equilibrium, the z -axis changes by angles $\sim 1\text{--}30$ over 20 Myr intervals, with changes larger than 10 degrees restricted to the earliest times, when the galaxy is closest to a spheroidal morphology (top panel of Fig. 4). During the steady phase, the change in orientation between snapshots is typically a degree or less, with larger peaks approaching 10 deg associated with the close approach of a merging companion.

APPENDIX C: COOLING TIME TO FREE-FALL TIME FOR EACH SIMULATION

Fig. C1 shows the ratio $t_{\text{cool}}^{(s)}/t_{\text{ff}}$ at $0.1R_{\text{vir}}$, defined in Stern et al. (2021a) and in Section 4.3, as a function of cosmic time. At late times when $t_{\text{cool}}^{(s)} \gg t_{\text{ff}}$ the inner CGM is dominated by a hot phase and is predominantly supported by thermal pressure, while at early times when $t_{\text{cool}}^{(s)} \ll t_{\text{ff}}$ the warm phase and kinetic pressure dominate (Figs 9–10). Comparing the intersection of the curves with the vertical line plotted at t_{bursty} reveals that inner CGM virialization coincides with the transitions we identify in the ISM, for all three simulations in our sample. The horizontal gray band in Fig. C1 corresponds to the range $t_{\text{cool}}^{(s)}/t_{\text{ff}} = 1\text{--}4$. The simple analytic expectation is that the CGM virializes when $t_{\text{cool}}^{(s)}/t_{\text{ff}}$ is of order unity, but Stern et al. (2021a) finds that for our exact definition of this ratio, the inner CGM in the FIRE simulations typically virializes when $t_{\text{cool}}^{(s)}/t_{\text{ff}}$ is in this range (see section 3.2 in Stern et al.).

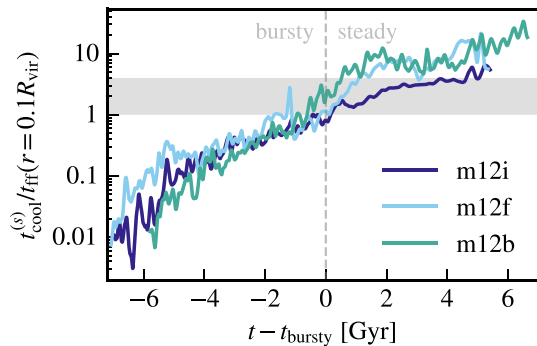


Figure C1. The ratio of the cooling time averaged over a thin shell at $0.1R_{\text{vir}}$ to the free-fall time versus cosmic time offset by t_{bursty} . The virialization of the inner CGM that occurs when $t_{\text{cool}}^{(s)}/t_{\text{ff}} \approx 1-4$ (Stern et al. 2021a) roughly coincides with t_{bursty} and the ISM transitions identified in this paper.

This paper has been typeset from a $\text{\TeX}/\text{\LaTeX}$ file prepared by the author.